Research Square

Preprints are preliminary reports that have not undergone peer review.
They should not be considered conclusive, used to inform clinical practice,
or referenced by the media as validated information.

Distinct lipid-binding sites coordinate claudin assembly and trafficking in tight junctions

Takehiro Shinoda

takehiro.shinoda@riken.jp

RIKEN Center for Integrative Medical Sciences https://orcid.org/0000-0003-0297-2471

Kenta Shigetomi

Faculty of Medical Sciences, Kyushu University

Masahiro Motohashi

RIKEN Pioneering Research Institute

Naoko Shinya

RIKEN Center for Integrative Medical Sciences

Kazushige Katsura

RIKEN https://orcid.org/0000-0002-4333-0224

Kazuharu Hanada

RIKEN Center for Integrative Medical Sciences

Tomomi Kimura-Someya

RIKEN Center for Integrative Medical Sciences

Masuo Kondoh

Osaka University

Junichi Ikenouchi

Kyushu University https://orcid.org/0000-0002-2936-3548

Yuji Sugita

RIKEN https://orcid.org/0000-0001-9738-9216

Mikako Shirouzu

RIKEN https://orcid.org/0000-0002-7997-2149

Article

Keywords:

Posted Date: November 19th, 2026

DOI: https://doi.org/10.21203/rs.3.rs-11517058/v1

License: This work is licensed under a Creative Commons Attribution 4.0 International License.
Read Full License

Additional Declarations: There is **NO** Competing Interest.

Distinct lipid-binding sites coordinate claudin assembly and trafficking in tight junctions

Authors: Takehiro Shinoda[1]*, Kenta Shigetomi[2], Masahiro Motohashi[3], Naoko Shinya[1], Kazushige Katsura[1], Kazuharu Hanada[1], Tomomi Kimura-Someya[1], Masuo Kondoh[4,5,6], Junichi Ikenouchi[2], Yuji Sugita[3,7,8], Mikako Shirouzu[1]*

Affiliations:

[1] Laboratory for Protein Functional and Structural Biology, RIKEN Center for Integrative Medical Sciences, 1-7-22 Suehiro-cho, Tsurumi-ku, Yokohama, Kanagawa 230-0045, Japan.

[2] Department of Biochemistry, Faculty of Medical Sciences, Kyushu University, Fukuoka, 812-8582, Japan.

[3] Theoretical Molecular Science Laboratory, RIKEN Pioneering Research Institute, Saitama 351-0198, Japan.

[4] Graduate School of Pharmaceutical Sciences, The University of Osaka, Osaka 565-0871, Japan.

[5] Global Center for Medical Engineering and Informatics, The University of Osaka, Suita, Osaka 565-0871, Japan.

[6] Center for Infectious Disease Education and Research, The University of Osaka, Suita, Osaka 565-0871, Japan.

[7] Computational Biophysics Research Team, RIKEN Center for Computational Science, Kobe 650-0047, Japan.

[8] Department of Physics, Faculty of Science and Engineering, Chuo University, Tokyo 112-8551, Japan.

*Correspondence to: E-mail: takehiro.shinoda@riken.jp (T.S.), mikako.shirouzu@riken.jp (M.S.)

Abstract

Tight junctions are essential for epithelial physiology, forming selective barriers that regulate paracellular transport and maintain tissue integrity. While claudins are recognized as their core structural components, how lipids contribute to tight junction architecture has remained a long-standing question. Here, we provide structural evidence for claudin–lipid interactions by determining the cryo-EM structure of claudin-4 bound to two distinct lipids, termed L1 and L2. At the L1 site, a long-chain sphingomyelin protruding along the extracellular domain is preferentially stabilized within ordered, thickened membranes, as supported by molecular dynamics simulations. At the L2 site, a phospholipid occupies the claudin dimer interface and may stabilize the dimeric conformation. Functional analyses of lipid-binding site mutants expressed in claudin-null cells revealed reduced localization of the L1-site mutant at apical tight junctions, whereas the L2-site mutant exhibited impaired plasma membrane translocation. Together, these findings support distinct but complementary roles for the two lipid-binding sites, with L1 promoting junctional localization in concert with claudin palmitoylation and L2 contributing to dimer stabilization. Our results provide a lipid-centered framework for understanding claudin organization beyond protein-protein interactions alone.

Main text

Introduction

The epithelial barrier prevents the entry of pathogens and regulates paracellular transport of ions and water, functions that are essential for multicellular life. These roles are mediated by tight junction strands (TJS), supramolecular assemblies primarily formed by claudins, tetra-spanning membrane proteins that interact in both cis and trans[1,2]. More than twenty claudin isoforms have been identified in humans, each conferring distinct barrier properties and exhibiting tissue-specific expression patterns[3].

Lipids are also thought to play important roles in TJS formation. Claudins and zonula occludens (ZO) proteins accumulate in cholesterol (CHOL)- and sphingomyelin (SM)-rich lipid rafts[4–6], and accumulating evidence highlights the contributions of CHOL, long-chain SM, and claudin palmitoylation to TJS organization[7,8]. Super-resolution microscopy has further revealed isoform-specific meshwork-like architectures of TJS[9], as well as interference and nanoscale segregation among claudin isoforms within junctional strands[9,10]. These morphological and functional characteristics have prompted efforts to reclassify claudin isoforms[9,11]. Nevertheless, the precise molecular contribution of lipids to claudin strand assembly remains unresolved.

At the structural level, since the crystal structure of mouse claudin-15 was

solved in 2014[12], structures of five additional claudin isoforms have been reported[13–16]. All share a conserved architecture, consisting of an extracellular domain composed of five β-strands and a transmembrane region containing four α-helices. However, no experimental structure of intact TJS has been reported to date. Based on crystal packing of claudin-15, the “joined double rows” (JDR) model was proposed, in which claudin molecules form linear-cis interactions within the same membrane plane, as inferred from the crystal lattice, and these parallel rows engage in trans interactions with opposing rows from the adjacent membrane, such that four claudins assemble to form a paracellular pore[17]. These structural insights, together with the JDR model, have markedly advanced our understanding of tight junction organization and enabled new approaches such as molecular dynamics simulations[18–24]. Despite these advances, all claudin structures reported to date were determined in detergent or crystalline environments and lack bound CHOL, SM, or any phospholipids. As a result, no direct structural evidence for specific claudin–lipid interactions has been obtained. Moreover, because the JDR model is composed exclusively of claudin molecules, it does not account for the well-documented involvement of lipids in TJS formation and stability. Thus, a central unresolved question remains: how do lipids contribute to the assembly and stabilization of tight junctions at the molecular level?

Cryo-electron microscopy (cryo-EM) offers a powerful means to address this question, as it enables visualization of membrane proteins together with associated lipids in near-native environments using saposin A nanoparticles[25]. Here, we report the cryo-EM structure of human claudin-4 bound to two lipids and demonstrate their distinct contributions to TJS organization through molecular dynamics (MD) simulations and functional assays in claudin-null cells.

Results

Cryo-EM reveals two lipid-binding sites in claudin-4

Human claudin-4 (hCLDN4) is a small membrane protein (~22 kDa) that presents inherent challenges for cryo-EM image processing. To facilitate structural analysis, hCLDN4 was prepared using an *Escherichia coli* cell-free protein synthesis system with lipid membranes[26] supplemented with polar lipid extracts from porcine brain and examined in complex with the Fab fragment of an anti-hCLDN4 monoclonal antibody, clone 5D12, which binds tightly to the extracellular domain of hCLDN4[27]. The resulting hCLDN4•Fab complex had a molecular mass of approximately 70 kDa. Detergent micelles surrounding the transmembrane (TM) region were replaced with saposin A nanoparticles[25] to prevent protein aggregation during vitrification. The cryo-

EM reconstruction at an overall resolution of 3.40 Å (Supplementary Fig. 1a, b) and the corresponding atomic model are shown in Fig. 1a–d. Stabilization of the extracellular domain by the Fab fragment and of the TM region by saposin A resulted in local resolutions exceeding 3.0 Å, particularly at the Fab–hCLDN4 interface and in the outer leaflet-facing regions of the TM helices (Supplementary Fig. 1c). Although full-length hCLDN4 was used for structure determination, the C-terminal region beyond Pro186 was poorly resolved (Supplementary Fig. 2a, b), consistent with the intrinsic flexibility of the cytoplasmic tails observed in other claudin structures[12,14–16]. Comparison with previously reported CLDN4 structures revealed that the TM helix arrangement of hCLDN4 in this study more closely resembled that of the AlphaFold2[28,29] apo model (AF-O14493-F1-model_v4) than that observed in the hCLDN4•C-CPE complex (PDB ID: 5B2G) (Supplementary Fig. 3a, d). The variable regions of the Fab heavy (VH) and light (VL) chains extensively contacted the V1 and V2 loops of the extracellular domain (Supplementary Fig. 4 and Supplementary Fig. 5a–d), thereby providing a structural basis for the high affinity (KD < 10 nM) and specificity of the 5D12 clone for CLDN4[27]. Consistent with this extensive interface, Fab binding displaced the V1 and V2 loops outward and induced pronounced reorientation of the side chains of Ser38, Asn39, Ile40, Val41 on the V1 loop, and Gln156 on the V2 loop (Supplementary Fig.

3b, c). In addition, densities corresponding to at least three saposin A molecules were observed surrounding the TM helices, although the resolution was insufficient for atomic-level refinement (Supplementary Fig. 6 a, b).

In the present cryo-EM map, two bound lipids, designated Lipid 1 (L1) and Lipid 2 (L2), were detected within the transmembrane region of hCLDN4 (Fig. 1b). At the L1 site, two straight densities oriented approximately perpendicular to the membrane were observed (Fig. 2a). These densities were consistent with hydrocarbon chains of approximately C18 and C22 in length, suggesting that L1 most likely corresponds to a sphingomyelin species containing a C22 N-acyl chain (hereafter referred to as C22 sphingomyelin). A notable feature of L1 was that it protruded above the predicted TM region along ECS1 (Fig. 2b and Supplementary Fig. 7). Residues located within 5 Å of L1 were distributed across TM helices α1 and α4 as well as the extracellular β-sheet (Fig. 2b, c). Together, these structural elements formed a shallow depression containing a negatively charged region near Ser43 and Thr45, into which the hydrophilic head group of L1 was oriented (Fig. 2c). Hydrophobic contacts were observed between the terminal portion of the N-acyl chain and Leu16 on α1, between the sphingosine acyl chain and Met29 on the α1–β1 loop, and between the membrane-interfacial region of the sphingoid backbone and Trp47 on the β2 strand (Fig. 2d).

Sequence alignment revealed poor conservation of the L1-binding residues across claudin isoforms, with relatively similar residues observed only among hCLDN3, 5, 6, and 9 (Fig. 3a and Supplementary Fig. 4).

At the L2 site, two elongated densities were observed. One density extended along the α2 helix and was consistent with a C16 acyl chain, whereas the second density bent markedly and extended toward the α1 helix, consistent with a C22 acyl chain. These features suggested that L2 most likely corresponds to a phospholipid containing a long unsaturated acyl chain (hereafter referred to as C16/C22 phospholipid) (Fig. 2e). Residues within 5 Å of L2 were located in TM helices α1 and α2 and in the extracellular β4–α2 loop, with Leu19 shared between the two lipid-binding sites (Fig. 2f, g). Narrow depressions formed by these residues accommodated the two acyl chains of L2 (Fig. 2g, h). At the membrane interface, Asp68 and Arg81 formed negatively and positively charged regions, respectively, positioning the polar head group of the lipid (Fig. 2g). Specific interactions were observed between Trp51 and the glycerol backbone, Arg81 and the phosphate group, and Ile85 and the C16 acyl chain (Fig. 2h). In contrast to the L1 site, residues constituting the L2 site were highly conserved, particularly in hCLDN1, 3, 5, 6, 7, 9, and 19 (Fig. 3b). In the crystal structure of mouse claudin-15 (mCLDN15), a glyceryl monoolein (OLC1) molecule has also been reported to occupy

the corresponding L2 site[12]. In CLDN4, the long acyl chain of L2 was bent at the position of Met22, whereas in CLDN15, in which the corresponding residue is Gly21, OLC1 extended linearly along the α1 helix. These differences suggest that Met22, together with Trp18, may contribute to the selection and arrangement of lipid hydrocarbon chains at the L2 site (Supplementary Fig. 8a–d).

Membrane properties differentially regulate lipid binding at the L1 and L2 sites

Next, we investigated the interactions between claudin and the two bound lipids, and their roles in TJS formation, using MD simulations[30–32]. Aligning our cryo-EM model with the JDR model proposed by Suzuki et al.[12,17] revealed steric clashes between adjacent hCLDN4 molecules and their bound lipids (Supplementary Fig. 9a–d), suggesting that lipid binding is incompatible with JDR assembly. We therefore constructed a face-to-face cis dimer model (Fig. 4a), representing half of the pore-forming unit of TJS[33], based on our hCLDN4 cryo-EM structure with palmitoyl chains introduced at five cysteine residues[34]. We then performed MD simulations under two membrane conditions: CHOL/SM (50 mol% CHOL and 50 mol% SM(d18:1/22:0)), reported to colocalize with claudins in plasma membranes[7], and a control 1-palmitoyl-2-oleoyl phosphatidylcholine (POPC)/ 1-palmitoyl-2-arachidonoyl-phosphatidylcholine

(PAPC) membrane (50 mol% each). We found that the face-to-face cis dimer was more stable in CHOL/SM than in POPC/PAPC, as measured by Cα RMSD and hydrogen bonds at the β4–β4 interface (Fig. 4b, c), whereas monomer stability was unchanged (Supplementary Fig. 10a, b). The head groups of L1 and L2 aligned with the thicker CHOL/SM membrane but protruded in POPC/PAPC, reflecting membrane thickness (Fig. 4d).

Focusing on the L1 and L2 lipids, the hydrophobic contact between L1 and Met29 was stable under CHOL/SM membrane conditions but was lost in one protomer under POPC/PAPC conditions (Fig. 5a). No persistent hydrogen bonds between L1 and claudin were observed under either condition (Fig. 5b), indicating that interactions at the L1 site are primarily mediated by contacts within the transmembrane region. RMSF analysis further showed smaller fluctuations in the hydrocarbon chains of L1 than in those of L2 (Supplementary Fig. 11a, b). In contrast, L2, which is located at the dimer interface, exhibited distinct interaction modes depending on membrane composition. Under POPC/PAPC conditions, stable hydrogen bonds were formed with Trp51, and interactions with Arg81 were maintained in one protomer. In the other protomer, the lipid dissociated from Arg81 and instead formed hydrogen bonds with Gln61 on the β4 strand of the opposing protomer. Under CHOL/SM conditions, hydrogen bonds with

Trp51 were lost, and interactions with Arg81 were weakened, whereas hydrogen bonding with Gln61 on the opposing protomer became dominant (Fig. 5c). These observations indicate that lipid binding at the L2 site adopts membrane composition-dependent interaction modes, and suggest that the Gln61-mediated interaction observed under CHOL/SM conditions contributes to stabilization of the dimer interface.

Beyond the L1 and L2 sites, lipid diffusion in the vicinity of the claudin dimer was markedly reduced under both CHOL/SM and POPC/PAPC membrane conditions (Supplementary Fig. 12a). Under CHOL/SM conditions, CHOL and SM accumulated at the dimer interface on the inner leaflet, where the palmitoylation sites on the α2–3 loop (P_{CL}) face each other (Supplementary Fig. 12b), consistent with previous simulations of palmitoylated claudin-5[35]. Under POPC/PAPC conditions, weak lipid stacking was also observed; however, the P_{CL}s were oriented outward rather than facing each other (Supplementary Fig. 12c), highlighting the importance of P_{CL} positioning for lipid accumulation. Similar phospholipid stacking at the dimer interface has also been reported in a previous MD study of a CLDN10b-based TJS model[21]. In addition, on the outer leaflet, CHOL preferentially bound near Gln78 and His141, with His141 forming stable hydrogen bonds with the CHOL hydroxyl group, whereas SM bound near Tyr148 and formed stable interactions via its head group under CHOL/SM conditions

(Supplementary Fig. 13a–c). Tyr148 was located at a similar z-position to the L1 head group. Under POPC/PAPC conditions, these residues interacted with POPC but not with PAPC (Supplementary Fig. 12d). Together, these observations suggest that these residues contribute to recognition of the membrane interface under both membrane conditions.

Two lipid-binding sites play distinct roles in claudin trafficking and tight junction localization

Finally, we investigated the functional significance of the two lipid-binding sites in TJS formation using claudin-null cells derived from mouse EpH4 cells[8]. As previously reported, CLDN4 fused to fluorescent proteins at the N-terminus does not efficiently form TJS[9,36]; therefore, untagged hCLDN4 was used in this study. Mutants targeting residues identified as lipid-interacting in the cryo-EM and MD analyses, Met29 at the L1 site and Arg81 at the L2 site, were expressed in these cells.

In the wild-type (WT) condition, expressed hCLDN4 efficiently translocated to the plasma membrane and localized to the apical region, where it colocalized with ZO-2 to form TJS (WT in Fig. 6a). In contrast, the Met29Ala mutant at the L1 site showed slightly reduced plasma membrane translocation and, even when present at the

membrane, exhibited a marked reduction in apical localization, remaining predominantly at the lateral membrane (M29A in Fig. 6a). By contrast, the Arg81Ala mutant at the L2 site showed a strong impairment in plasma membrane translocation (R81A in Fig. 6a). Instead, the majority of the mutant protein accumulated in the cis-/medial-Golgi, rather than in lysosomes or early endosomes (Fig. 6b–d), suggesting a defect in trafficking from the cis-/medial-Golgi to the trans-Golgi/trans-Golgi network (TGN) compartments.

Together, these results demonstrate that the two lipid-binding sites on CLDN4, identified by cryo-EM and shown to exhibit distinct behaviors in MD simulations, play clearly differentiated roles: the L1 site contributes to apical tight junction localization, whereas the L2 site is essential for intracellular trafficking of claudin to the plasma membrane.

Discussion

In this study, we provide direct structural evidence for claudin–lipid interactions by determining the cryo-EM structure of hCLDN4 bound to two distinct lipids, termed L1 and L2. By integrating cryo-EM, MD simulations, and cell-based analyses, we show that these lipids contribute to distinct aspects of claudin behavior,

with L2 potentially contributing to cis-dimer stabilization and playing a role in early membrane trafficking, whereas L1 contributes to efficient apical localization. How lipid binding at the L1 site relates to higher-order tight junction strand organization is discussed below.

Classification of claudin isoforms based on two lipid-binding sites

As described above, residues forming the L1 site of hCLDN4 showed sequence similarity to those of the other barrier-forming claudins, hCLDN3, 5, 6, and 9 (Fig. 3a). In particular, the conservation of Met29 and ECS1 in hCLDN3 and hCLDN5 strongly suggests that the L1 site is conserved in these isoforms, not only in terms of the bound lipid species, likely a long-chain sphingomyelin, but also in the mode of interaction observed in hCLDN4. Consistent with this idea, the behaviors of L1 observed in our MD simulations and cell-based assays are likely shared, at least in part, among these isoforms. Notably, in our MD simulations, no persistent hydrogen bonds were detected between the L1 head group and the extracellular domain under either membrane condition (Fig. 5b), suggesting that interactions involving the L1 head group are relatively weak or transient. This suggests that, in CHOL/SM-rich membrane environments, interactions between claudin and L1 are maintained primarily within the

membrane, whereas the L1 head group retains a considerable degree of positional freedom. Such a property is also likely conserved, at least among these isoforms. As discussed below in the context of the proposed strand model, we suggest that the L1 head group can participate in linear-cis interactions. The conformational flexibility of the L1 head group may therefore contribute to the permissiveness required for heterophilic interactions among different claudin isoforms.

In contrast, the L2 site is highly conserved across claudins and contains a canonical phospholipid interaction motif involving Trp51 and Arg81 at the membrane interface[37] (Fig. 3b). The conservation of these residues, together with structural similarities to mCLDN15 (Supplementary Fig. 8c, d), suggests that lipid binding and head-group recognition mechanisms at the L2 site may be broadly conserved. Arg81, conserved in nearly all claudins except CLDN2 and CLDN12, has been shown to be required for efficient plasma membrane translocation when mutated[38–41], further supporting a conserved functional role of L2-mediated lipid interaction.

Comparison of lipid-binding site conservation with previously reported functional classifications[9,11] reveals notable correlations (Fig. 3a, b). Isoforms showing high sequence similarity to CLDN4 (CLDN1, 3, 5, 6, 7, 9, and 19) are all classified as autonomous barrier-forming claudins[11]. Of these, isoforms exhibiting particularly high

similarity also show a degree of correspondence with classifications based on tight junction meshwork morphology[9]. Autonomous channel-forming claudins and nonautonomous barrier-forming claudins also appear to exhibit similar tendencies, although these correlations are less pronounced than those observed for barrier-forming claudins. The relationships with these classifications differ slightly between the L1 and L2 sites: the L1 site shows a pattern more similar to classifications based on meshwork morphology, whereas the L2 site more closely reflects classifications based on barrier function and strand-forming ability. These observations suggest that the L1 and L2 sites play distinct roles in TJS formation and function, and that these tendencies are shared among claudin isoforms according to sequence similarity at the respective lipid-binding sites. Further systematic identification of lipid species bound to individual claudin isoforms will be required to clarify how lipid binding contributes to tight junction function and architecture.

Lipid environment-dependent claudin translocation and TJ localization

A previous study has shown that claudins harbor two cytoplasmic palmitoylation sites, P_{CL} (Cys104/107 in hCLDN4) and P_{TM} (Cys182/183/185 in hCLDN4), which, in concert with transmembrane helices, confer distinct lipid

preferences and thereby generate an asymmetric lipid membrane environment with different degrees of membrane order and thickness surrounding individual claudin molecules[35]. Fig. 7a schematically illustrates a face-to-face cis claudin dimer, integrating the lipid preferences identified in these prior studies with the L1/L2 lipid-binding sites and the two palmitoylation sites characterized in the present work. As shown in this model, formation of the face-to-face cis dimer consolidates the lipid preferences of claudin into two principal directions around the dimer.

One of these directions corresponds to a preference for a highly ordered and thick membrane environment, where the P_{CL} is located. Notably, this direction coincides with the position of the L1 lipid-binding site identified in our cryo-EM structures, where long-chain SM was resolved. Consistent with this correspondence, MD simulations showing stable interactions between claudin and L1 lipids under CHOL/SM membrane conditions (Fig. 5a). In our cell-based assays, mutation of Met29 at the L1 site resulted in claudins that reached the lateral membrane but failed to translocate to the apical domain (Fig. 6a), a phenotype strikingly similar to that reported for palmitoylation-deficient claudin mutants[8,34,42]. Taken together, these observations suggest that the L1 site contributes to lipid environment formation in the upper leaflet, whereas palmitoylation modulates the lower leaflet, thereby collectively promoting affinity

between (likely face-to-face cis-dimerized) claudins and highly ordered, thick membranes enriched in CHOL and SM. This affinity, in turn, likely provides a driving force for claudin localization to the CHOL/SM-rich apical membrane[43,44] (Fig. 7b).

Because lipid preferences around a face-to-face cis dimer are concentrated in two directions (Fig. 7a), claudin dimers arriving at the apical membrane may further assemble and align in response to the surrounding lipid environment. This interpretation is consistent with previous reports demonstrating a strong correlation between CHOL/SM content and claudin apical targeting and tight junction strand formation[7]. Furthermore, the phenotypes observed for L1-site mutants in our cell-based assays support the idea that L1-bound lipids contribute to lipid affinity and orientation around the face-to-face cis dimer (Figs. 6a and 7a). Given that the amino acid compositions of the L1 and L2 sites correlate with tight junction meshwork morphology and functional differences among claudin isoforms (Fig. 3a, b), these correlations suggest that lipid preferences around face-to-face cis dimers may exhibit isoform-specific features. We therefore propose that individual claudin isoforms preferentially recruit and surround themselves with distinct lipid environments and tend to cluster with other isoforms sharing similar lipid preferences. Such isoform-dependent lipid affinities may be important determinants of claudin sorting after apical delivery, as well as of inter-

claudin interference[10] and nanoscale segregation within tight junction meshworks[9].

In contrast, the L2 lipid is positioned at the dimer interface within the face-to-face cis claudin dimer (Figs. 4a and 7a). In our MD simulations, L2–claudin interactions were enhanced under POPC/PAPC membrane conditions, in clear contrast to L1 (Fig. 5c). In our cell-based analyses, an Ala mutation of Arg81 at the L2 site markedly impaired claudin translocation to the plasma membrane, resulting in its retention within the cis-/medial-Golgi membranes (Fig. 6a–d). Under CHOL/SM membrane conditions, MD simulations further revealed enhanced hydrogen bond formation between the L2 lipid headgroup and Gln61 on the β4 strand of the adjacent claudin protomer (Fig. 5c). This interaction is likely facilitated by membrane thickening, which brings the L2 headgroup closer to Gln61, and may contribute to stabilization of the dimeric architecture observed under CHOL/SM conditions (Fig. 4b, c). The dimer interface also harbors the P_{CL} site, which is associated with a preference for thick, highly ordered membranes (Fig. 7a). In MD simulations under CHOL/SM conditions, CHOL stacking was observed on both the outer and inner leaflets surrounding this interface (Supplementary Fig. 12b and Supplementary Fig. 13a, c), suggesting that the region encompassing the L2 site and the dimer interface is predisposed to forming a highly ordered and thick lipid membrane environment. Together, these observations indicate a

strong correlation between membrane thickness and stabilization of the claudin dimer structure.

In light of the progressive changes in membrane composition and thickness from the endoplasmic reticulum (ER) to the trans-Golgi/TGN, our findings suggest that lipid binding at the L2 site occurs at relatively early post-translational stages within thin ER or cis-Golgi membranes. As claudins progress toward the trans-Golgi/TGN and encounter progressively thicker membranes, formation of the face-to-face cis dimer may be promoted. Hydrogen bond formation between the L2 lipid and Gln61 on the adjacent protomer (Fig. 5c) is likely facilitated during this transition. Because lipid binding at the L1 site is also favored in thick membrane environments, L1 lipids may become more stably associated with claudins as they reach trans-Golgi/TGN membranes, where SM synthesis takes place. Moreover, the retention of the Arg81Ala mutant within cis-/medial-Golgi membranes (Fig. 6a) raises the possibility that lipid binding at the L2 site and dimer-mediated structural stabilization contribute to a quality-control process associated with trafficking from the cis-/medial-Golgi to the trans-Golgi/TGN.

A tight junction strand model incorporating two lipid-binding sites

The prevailing JDR model proposed by Suzuki and its derivative models

describe TJS formation as the linear-cis alignment of face-to-face claudin dimers, mediated by interactions between hydrophobic residues on the extracellular helix (ECH) of one claudin and aromatic residues near the tip of the α3 helix of an adjacent claudin[12,17] (Supplementary Fig. 9a). However, as described above, in hCLDN4 bound to L1 and L2 lipids, alignment along the linear-cis direction according to the JDR model results in steric clashes because the L1 lipid interferes with neighboring protomers (Supplementary Fig. 9b–d). In addition, our MD simulations show that SM stacks onto Tyr148, an aromatic residue near the extracellular tip of the α3 helix that is considered critical for linear-cis interactions in the JDR model (Supplementary Fig. 13b, c), thereby further limiting potential interactions between this region and the ECH of adjacent claudins.

Although the intrinsic ability of CLDN4 to form tight junction strands autonomously remains debated, multiple studies agree that, compared with other claudin isoforms, CLDN4 alone is inefficient at spontaneous strand formation[9,11,22,36,45]. Consistent with this notion, our observations using non-epithelial L929 cells revealed accumulation of CLDN4 at cell–cell contacts, but no meshwork-like tight junction strand structures were detected (Supplementary Fig. 14a, b). Furthermore, CLDN4 has been reported to behave antagonistically toward channel-forming claudins within tight

junctions[10]. Taken together, it is therefore not unexpected that the JDR model, originally developed for mCLDN15, cannot be directly applied to CLDN4, and the possibility that CLDN4 adopts a distinct strand organization cannot be excluded. The JDR model was validated primarily using phenotypes observed in Sf9 cells[12,17], which contain very low levels of CHOL[46–48], whereas similar phenotypes have not been observed in mammalian cells[39]. Together, these observations suggest that alternative strand models incorporating bound lipids, including L1 and L2, as well as the surrounding membrane environment, may warrant consideration.

As discussed above, the face-to-face cis dimer exhibits two preferential directions of lipid membrane affinity, which are expected to differ among claudin isoforms. Isoforms sharing similar lipid preferences may therefore spontaneously cluster and align in a defined orientation. Based on this assumption, we arranged tetramers, minimal functional units of barrier- or channel-forming claudins composed of two face-to-face cis dimers paired in trans, in a linear fashion along the membrane plane. This arrangement yields an octameric strand model (Fig. 8a and Supplementary Fig. 15a). In this hypothetical model, linear-cis interactions are mediated primarily by hydrophobic contacts between conserved residues Ile36, Ile40, and Val41 on V1 of ECS1, which are well preserved among claudin isoforms capable of spontaneous strand

formation[9,11] and are oriented outward in the cryo-EM structure determined in this study (Supplementary Fig. 3c and Supplementary Fig. 4). Consequently, complex interactions requiring large conformational rearrangements are not necessary (Fig. 7b–d, Supplementary Fig. 15b, c).

Importantly, the L1 lipid, which caused steric clashes in the JDR-type alignment (Supplementary Fig. 9b–d), can participate in linear-cis interactions around this hydrophobic patch in the present model (Supplementary Fig. 15b, c). Moreover, adjacent units interact along surfaces that preferentially associate with thick, highly ordered membranes, where the L1 site and the P_{CL} are located (Fig. 7a and Fig. 8e). As a result, the inter-unit spaces are filled with CHOL- and SM-rich, thick, and highly ordered membranes (Fig. 8f). Aromatic residues near the tip of the α3 helix, previously proposed as key mediators of linear-cis interactions in the JDR model[12,17], are also located on this surface. Considering our MD results (Supplementary Fig. 13b, c), these residues are more likely to function as membrane interface anchors that help maintain local membrane thickness rather than as direct protein–protein interaction sites.

Tight junction strands form curved, meshwork-like assemblies composed of multiple claudin isoforms, and their morphology and composition dynamically change in response to external factors such as osmotic stress and pH[11,49–51]. Moreover, tight

junction strands are highly sensitive to lipid composition, as evidenced by their reversible disruption and reassembly upon CHOL depletion or supplementation[4,7,8]. The MD simulations of the JDR model comprising 300 CLDN15 molecules have indicated that linear-cis interactions between units are variable[23]. Given this intrinsic flexibility and strong dependence on the lipid membrane environment, a flexible strand model based on simple and permissive linear-cis interactions, rather than rigid protein-centric interfaces, appears plausible.

Recently, cryo-electron tomography analysis of TJSs formed by hCLDN15 expressed in MDCK II cells lacking CLDN1–4 and CLDN7 has been reported[52]. Although a full three-dimensional reconstruction was not achieved, the study provided more quantitative information regarding strand dimensions and spatial organization than previously available. According to that report, the membrane thickness in TJSs formed by hCLDN15 was approximately 40 Å, and the paracellular space width was also approximately 40 Å. In contrast, our hypothetical strand model based on hCLDN4 predicts a membrane thickness of approximately 50 Å and a paracellular space width of approximately 20 Å (Fig. 8a), indicating substantial differences between the two systems. As demonstrated by our MD simulations, the membrane thickness surrounding claudin molecules reflects the positioning of the L1 and L2 lipids (Fig. 4d). Moreover,

given that the amino acid composition of the L1 site differs markedly between channel-forming CLDN15 and barrier-forming CLDN4, these structural differences may arise from differences in the lipid species accommodated at the L1 site and/or in their modes of interaction. Furthermore, such variations in membrane thickness may be closely related to interclaudin interference[10] and segregation[9] during tight junction strand formation.

Because the present strand model remains insufficiently validated, further experimental testing, particularly in cellular systems, will be required, and a more comprehensive evaluation will be reported elsewhere.

Limitations and future perspectives

Despite the insights gained, several limitations should be noted. Although we attempted to identify lipid species at the L1 and L2 sites by LC–MS, definitive assignment was not achieved, likely due to co-purified heterogeneous lipids and technical limitations in extraction and detection. Thus, the lipids used in cryo-EM analyses and MD simulations were inferred from density features rather than directly identified endogenous ligands. While these models reproduce key physicochemical characteristics, the precise acyl chain composition and head groups of native lipids may

differ. In addition, MD simulations are limited by force-field accuracy and simulation timescales, and therefore cannot fully capture claudin–lipid interactions in the complex cellular membrane environment. Dynamic processes such as lipid exchange, membrane remodeling, and interactions with other tight junction components were not addressed.

Future refinement of lipid-dependent tight junction models will require direct in situ visualization of tight junction strands. Cryo-electron tomography combined with subtomogram averaging offers a promising strategy to resolve the native organization of claudin isoforms and associated lipids. Systematic identification of bound lipids across isoforms will also be essential to define isoform-specific lipid preferences and their roles in strand assembly and barrier function.

In conclusion, this study identifies two lipid-binding sites on hCLDN4 and provides evidence for their complementary roles in tight junction biology, with L1 contributing to apical tight junction localization and L2 potentially stabilizing the face-to-face cis dimer. Although CHOL- and SM-rich membrane environments have long been implicated in claudin localization and strand formation, direct structural evidence linking specific lipid interactions to claudin function has remained limited[4,6–8,20,26,35]. By filling this gap, our findings establish a lipid-centered framework for understanding

tight junction organization beyond protein–protein interactions alone. Furthermore, the observation that several disease-associated mutations map to transmembrane regions outside the L1 and L2 sites raises the possibility that additional lipid-binding sites may contribute to claudin trafficking and tight junction localization[38,40,53–57] (Supplementary Fig. 16a–e). Together, these findings highlight lipid–protein interactions as integral determinants of claudin function and tight junction architecture and lay a foundation for future studies aimed at elucidating lipid-dependent mechanisms underlying epithelial barrier regulation and claudin-associated diseases.

Materials and Methods

Materials

Digitonin (044-02121) was purchased from FUJIFILM Wako Chemicals Industries. Cholesteryl hemisuccinate (CHS; CH210) and n-dodecyl-β-D-maltopyranoside (β-DDM; D310) were obtained from Anatrace. Porcine brain polar lipid extract (141101) was purchased from Avanti Polar Lipids. Reagents and tools for X-ray crystallography were obtained from Hampton Research and Molecular Dimensions. QUANTIFOIL holey carbon grids (R0.6/1.0, 300-mesh copper) were purchased from Quantifoil Micro Tools GmbH. Monoclonal antibodies (mAbs) for immunofluorescence were purchased from Cell Signaling Technology (anti-LAMP1 mAb, 99437; anti-RCAS1 mAb, 12290; and anti-EEA1 mAb, 3288) and Thermo Fisher Scientific (anti-claudin-4 mAb, 34-9400; anti-ZO-2 polyclonal antibody, 711400). All other chemicals used for protein sample preparation were purchased from Nacalai Tesque. The cDNA clone encoding human claudin-4 (O14493) was obtained from the Research Association for Biotechnology. The cDNA clone encoding human saposin A (P07602) was kindly provided by the Kazusa DNA Research Institute.

Expression and purification of saposin A

Expression vectors for human saposin A (residues 60–140), fused at the N-terminus to a six-histidine affinity tag, were constructed in the pET-28 vector (Novagen). Expression and purification of saposin A followed previous reports[25]. Briefly, *Escherichia coli* Rosetta-gami2 (DE3) cells harboring the plasmid were disrupted by sonication in lysis buffer [20 mM HEPES-NaOH (pH 7.5), 20 mM imidazole, 150 mM NaCl], and the supernatant was collected after centrifugation at 15,000 rpm. The supernatant was heat-treated at 85 °C for 10 min, centrifuged again at 15,000 rpm, and the resulting supernatant was purified using a HisTrap HP affinity column (Cytiva). Finally, the eluate was fractionated by size-exclusion chromatography on a HiLoad 16/60 Superdex 200 column (Cytiva) in running buffer [20 mM HEPES-NaOH (pH 7.5), 150 mM NaCl], and the monodisperse peak fraction was collected and used for saposin A nanoparticle preparation.

Expression and purification of the Fab fragment of anti-human claudin-4 antibody

For preparation of the Fab fragment used for model refinement of the $P4_12_12$ crystal structure and for cryo-EM analysis, a human embryonic kidney (HEK) cell expression system was used. Expression vectors were constructed for the variable region of the heavy chain (VH, residues 1–113) of the anti-human claudin-4 antibody

clone 5D12[27], fused at the C-terminus to the heavy-chain constant region (CH) of Herceptin[58] via a tobacco etch virus (TEV) protease recognition site and a six-histidine affinity tag separated by a Thr-Val-Ser-Ser-Ala linker. A corresponding vector encoding the light-chain variable region (VL, residues 1–108) fused to the light-chain constant region (CL) of Herceptin was also generated. Both constructs were cloned into pcDNA3.4 using TOPO cloning (Life Technologies, USA). Large-scale production of the Fab fragment was carried out in Expi293 cells. Plasmids encoding the heavy and light chains were co-transfected into HEK cells at a 3:1 ratio, and the cells were incubated at 37 °C for 72 h. The culture supernatant containing the secreted Fab fragments was collected and applied to Ni-Sepharose resin (GE Healthcare Life Sciences). The resin was washed with 20 column volumes of buffer [50 mM Tris-HCl (pH 7.0), 400 mM NaCl], and bound proteins were eluted with five column volumes of the same buffer supplemented with 500 mM imidazole. The Fab fragments were further purified by size-exclusion chromatography on a HiLoad 16/60 Superdex 200 column (GE Healthcare Life Sciences) equilibrated in running buffer [50 mM Tris-HCl (pH 7.0), 400 mM NaCl], yielding a monodisperse peak.

Fab fragments used to prepare $P2_12_12_1$ crystals for initial model building were produced using an *E. coli* cell-free protein synthesis system[59,60]. Expression constructs

encoding the heavy and light chains were generated as chimeras with the same Herceptin CH and CL regions as described above. In these constructs, a modified natural polyhistidine tag (N11; MKDHLIHNHHKHEHAHAEH), a TEV protease recognition site, and a GSSGSSG linker sequence[61] were fused to the N terminus of each chain. The proteins were synthesized at 25 °C for 5 h using a previously reported *E. coli* cell-free antibody production method[62]. The reaction mixture was centrifuged at 15,000 × *g*, and the supernatant was collected for purification. Subsequent purification was performed under the same conditions as described for the HEK-expressed Fab fragments.

Cell-free production of human claudin-4 and purification of the complex with Fab fragment and saposin A nanoparticle

The expression vector for full-length human claudin-4, fused at the N-terminus with an N11 tag, a TEV protease recognition site, and the linker sequence GSSGSSG, was constructed by TOPO cloning (Life Technologies, USA). Human claudin-4 was synthesized with the *E. coli* cell-free protein synthesis system using the soluble-membrane fragment method[26] in the presence of mixed micelles containing 3.3 mg/ml lipids [10% (w/w) CHOL and 90% (w/w) porcine brain polar lipid extract] and 10.0

mg/ml digitonin. Following synthesis, claudin-4 was recovered from the 100,000 × *g* supernatant, bound to Ni-Sepharose affinity resin, washed with buffer [50 mM Tris-HCl (pH 7.0), 0.05% βDDM, 0.002% CHS, 20 mM imidazole, 400 mM NaCl], and eluted with 500 mM imidazole in the same buffer. The N-terminal N11 tag was removed by overnight digestion at 4 °C with His-tagged TEV protease while dialyzing against buffer [50 mM Tris-HCl (pH 7.0), 0.05% βDDM, 0.002% CHS, 400 mM NaCl]. The N11 tag fragment and His-tagged TEV protease were removed by immobilized metal affinity chromatography (reverse IMAC), and tag-free claudin-4 was recovered in the flow-through and wash fractions. The resulting claudin-4 was mixed with purified Fab fragments of anti-human claudin-4 antibody in excess and incubated at 4 °C for 1 h to form the claudin-4–Fab complex. The complex was captured on Ni-Sepharose resin via the C-terminal 6×His tag of the Fab fragment, washed, and eluted. As before, the 6×His tag of the Fab was removed by TEV protease digestion at 4 °C overnight during dialysis. The His-tag fragment and His-tagged TEV protease were removed by reverse IMAC, and the tag-free claudin-4–Fab complex was recovered in the flow-through and wash fractions. The complex was further purified by size-exclusion chromatography (Superdex 200 Increase 10/300) in running buffer [50 mM Tris-HCl (pH 7.0), 0.05% βDDM, 0.002% CHS, 150 mM NaCl], yielding a monodisperse peak corresponding to

the protein complex. For reconstitution with saposin A nanoparticles, the purified claudin-4–Fab complex was incubated with porcine brain polar lipid extract at a 1:1 (w/w) ratio at 4 °C for 30 min, followed by the addition of purified His-tagged saposin A at a 1:2 (w/w) ratio and incubation at 4 °C for ~2 h. The mixture was bound to Ni-Sepharose resin via the N-terminal 6×His tag of saposin A, washed with detergent-free buffer [50 mM Tris-HCl (pH 7.0), 20 mM imidazole, 150 mM NaCl], and eluted with 500 mM imidazole in the same buffer. The reconstituted claudin-4–Fab complex in saposin A nanoparticles was further purified by size-exclusion chromatography (Superdex 200 Increase 10/300) in running buffer [50 mM Tris-HCl (pH 7.0), 150 mM NaCl], yielding a monodisperse peak corresponding to the protein complex, which was immediately used for cryo-EM grid preparation.

Crystallization and data collection of the Fab fragment of anti-hCLDN4 antibody

Purified Fab fragments were concentrated to 10–20 mg/ml and mixed in a 1:1 ratio with reservoir solution. For crystals in the $P4_12_12$ space group, the reservoir solution consisted of 0.5 M sodium citrate buffer (pH 8.4) containing 0.09 M imidazole. For crystals in the $P2_12_12_1$ space group, the reservoir solution contained 0.1 M imidazole (pH 6.9), 30% (w/v) PEG 8000, and 0.2 M NaCl. Crystallization was carried

out by the hanging-drop vapor diffusion method at 15 °C. Crystals appeared within a few days and grew to dimensions exceeding 100 × 100 × 100 μm³ within approximately one week.

$P4_12_12$ crystals were soaked in reservoir solution supplemented with 15% (w/v) sucrose for 45 min, mounted in cryo-loops, and flash-cooled in liquid nitrogen. In contrast, $P2_12_12_1$ crystals were mounted directly from the drop and flash-cooled without additional cryoprotection. X-ray diffraction data were collected at beamline BL26B2 at SPring-8 using an MX225HE CCD detector under a 100 K nitrogen cryostream. For each crystal, 720 diffraction images were recorded over a total rotation range of 360° with an oscillation angle of 0.5° per image at a wavelength of 1.0000 Å. Diffraction data were processed using XDS[63]. The space group and unit cell parameters were determined using POINTLESS from the CCP4 suite[64]. The unit cell dimensions were as follows: $P4_12_12$, $a = b = 93.0$ Å, $c = 106.0$ Å; $P2_12_12_1$, $a = 93.8$ Å, $b = 99.7$ Å, $c = 104.8$ Å.

Phasing of X-ray diffraction data, model building, and refinement

Phasing, model building, and refinement were carried out using the Phenix suite[65] and Coot[66]. For the 2.4 Å resolution dataset obtained from $P2_12_12_1$ crystals, molecular replacement was performed with Phaser-MR[67] implemented in Phenix using

the coordinates of Herceptin (PDB ID: 1N8Z) as the search model. The resulting phases were used for automated model building with AutoBuild in Phenix, followed by manual model correction in Coot to generate an initial model. Subsequently, the 1.6 Å resolution dataset from $P4_12_12$ crystals was phased by molecular replacement with Phaser in Phenix using the initial model derived from the $P2_12_12_1$ crystal as the search model. The structure was refined using phenix.refine in the Phenix suite with iterative manual rebuilding in Coot (Supplementary Table 1). Model quality was assessed using MolProbity[68]. The Ramachandran statistics were 95.84% favored, 4.16% allowed, and 0.00% outliers. Rotamer outliers accounted for 1.06%, and the clashscore was 3.96. The final R_{work} and R_{free} values were 0.227 and 0.268, respectively.

Cryo-EM data acquisition

A 4-μl aliquot of the protein sample was applied to a glow-discharged grid (R0.6/1.0, 300-mesh copper; Quantifoil Micro Tools GmbH), blotted for 3 s at 4 °C under 100% humidity, and plunge-frozen in liquid ethane using a Vitrobot Mark IV (Thermo Fisher Scientific). Data were collected on a Titan Krios G4 electron microscope (Thermo Fisher Scientific) operated at 300 kV and equipped with a K3 direct electron detector (Gatan, Pleasanton, CA, USA) in counting mode. A total of

4,933 movies were recorded at a nominal magnification of ×105,000, corresponding to a calibrated pixel size of 0.8285 Å at the specimen level. The defocus range was −0.8 to −2.2 μm, and the total electron exposure was approximately 50 $e^{-}/Å^{2}$.

Cryo-EM single-particle analysis

Movie frames acquired in this study were motion-corrected using RELION 3.1.3[69]. Subsequent single-particle image processing was performed with cryoSPARC v3.2.0 and v4.7.1[70] (CryoEM Solutions Inc., Toronto, ON, Canada). The overall workflow is summarized in Supplementary Fig. 2a. Motion-corrected micrographs were imported into cryoSPARC and subjected to CTF estimation. Particles were initially picked using the Blob picker and extracted for two-dimensional (2D) classification. Well-defined 2D class averages corresponding to the claudin-4 complex were selected as templates for template-based particle picking. The repicked particles were extracted and subjected to additional 2D classification, and only classes exhibiting clear structural features of the claudin-4 complex were retained.

For volume-based particle sorting, iterative rounds of ab initio reconstruction and heterogeneous refinement were performed. Major classes were selected based on map quality and estimated resolution until approximately 100,000 particles remained.

Non-uniform refinement was then carried out with *C*1 symmetry imposed, using an automatically generated mask. After the global resolution improved beyond 4 Å, Patch CTF refinement was performed to optimize CTF parameters across the dataset. The particles were subsequently subjected to additional rounds of ab initio reconstruction and non-uniform refinement, followed by Local CTF refinement to correct per-particle defocus variation. A further round of ab initio reconstruction and heterogeneous refinement with a maximum resolution limit of 3.5 Å was conducted to remove remaining heterogeneity, and the selected particles were refined by non-uniform refinement to yield the final reconstruction. The final map reached a global resolution of 3.40 Å based on 106,211 particles, as estimated by the gold-standard Fourier shell correlation (FSC) using the 0.143 criterion (Supplementary Fig. 1b). For model building, the final map was sharpened in cryoSPARC using a *B*-factor of −148.5 Å^2.

Model building and refinement

The initial model consisted of the AlphaFold2 model of human claudin-4 (AF-O14493-F1-model_v4) and the X-ray crystal structure of the Fab fragment of the anti-hCLDN4 antibody described above (PDB ID: 24LZ). Two bound lipid molecules were generated using phenix.elbow in the Phenix suite: SM(d18:1/22:0), modeled as a

C22 sphingomyelin at the L1 site, and PC(16:0/22:6), modeled as a C16/C22 phospholipid at the L2 site.

Rigid-body fitting of the AlphaFold2 model, the Fab fragment, and the two lipid molecules was performed against the sharpened non-uniform refinement map using UCSF Chimera[71]. The model was subsequently manually adjusted in Coot according to the density and refined using real-space refinement in the Phenix suite with secondary-structure restraints applied throughout refinement. To further improve map quality, local refinement was performed using a reference map and a focal mask derived from the initial model. The resulting map was processed using DeepEMhancer[72] in cryoSPARC with a tight target model. The protein model was iteratively rebuilt in Coot and refined in real space in Phenix against the DeepEMhancer map to improve geometry and map fit. Finally, the complex model was re-refined against the sharpened non-uniform refinement map, focusing primarily on optimizing the map fit of the two bound lipid molecules with appropriate geometry restraints applied (Supplementary Fig. 2a).

Model validation was performed using MolProbity. The Ramachandran statistics were 97.08% favored, 2.92% allowed, and 0.00% outliers. Rotamer outliers accounted for 2.49%, and the clashscore was 7.92. The map–model FSC at the 0.5

criterion was 3.86 Å (Supplementary Table 2).

Face-to-face dimer model and proposed octameric strand model of human claudin-4 with two bound lipids

The face-to-face dimer model used for MD simulations was constructed based on a previously reported model. Our human claudin-4 structure was aligned to the JDR strand model reported by Suzuki et al.[17] using PyMOL (Schrödinger, LLC). The model was manually adjusted using Coot and UCSF Chimera to allow the formation of four hydrogen bonds between the opposing β4 strands. The resulting model was subjected to map-independent geometry minimization using the geometry minimization module in the Phenix suite, with non-crystallographic symmetry (NCS) and secondary-structure restraints applied.

The proposed octameric strand model was generated by first arranging two face-to-face dimer models in a head-to-head trans configuration, ensuring close packing without steric clashes, in the same manner as described for the face-to-face dimer modeling. The dimers were subsequently aligned in the linear-cis direction such that the hydrophobic patches of the V1 regions faced each other. The assembled model was then subjected to geometry minimization with NCS and secondary-structure restraints

applied.

Molecular dynamics simulation in lipid bilayer

Initial structures for the MD simulations were prepared from the previously constructed face-to-face hCLDN4 dimer model containing the bound lipids L1 and L2. Subsequent system preparation was carried out using VMD software[73]. Intramolecular disulfide bonds were formed between residues 54 and 64 within each subunit, and S-palmitoylation was introduced at cysteine residues 104, 107, 182, 183, and 185 located near the membrane interface. The modified structures, retaining the bound lipids, were embedded in lipid bilayers to generate membrane–protein complex systems. The CHARMM36m force field[74], including compatible lipid parameters, was employed. Two membrane compositions were used: a bilayer containing 50 mol% cholesterol (CHOL) and 50 mol% sphingomyelin [SM(d18:1/22:0)], and a bilayer containing 50 mol% 1-palmitoyl-2-oleoyl-sn-glycero-3-phosphocholine (POPC) and 50 mol% 1-palmitoyl-2-arachidonoyl-sn-glycero-3-phosphocholine (PAPC). The hCLDN4 dimers embedded in each membrane were solvated with CHARMM TIP3P water[75] in a periodic simulation box with dimensions of 120 × 120 × 102 Å^3. The systems contained approximately 150 mM NaCl and approximately 130,000 atoms in total.

Subsequently, molecular dynamics simulations were performed for both membrane systems (CHOL/SM and POPC/PAPC) using an identical protocol. Energy minimization was first carried out using the steepest descent method. This was followed by 9.6 ns of equilibration, during which the ensemble, time step, integration scheme, and restraint conditions were changed stepwise. In the initial stage, simulations were conducted in the NVT ensemble with a time step of 1 fs, with positional restraints applied to the protein backbone atoms, side chains, and bound lipids. Distance restraints were also imposed to maintain specific protein–lipid and inter-subunit interactions. As equilibration progressed, the ensemble was switched to the NPT ensemble, the time step was gradually increased from 1 fs to 2 fs and then to 2.5 fs, and the restraint force constants were progressively reduced until all restraints were removed.

Production simulations were then performed in the NPT ensemble at 300 K and 1 atm. Temperature and pressure were controlled using the stochastic velocity-rescaling thermostat[76] and the MTK barostat[77], respectively, under semi-isotropic conditions, using the refined temperature definition[78]. Temperature and pressure were evaluated using group-based definitions[79,80]. Water molecules were treated as rigid bodies using the SETTLE algorithm[81], while bonds involving hydrogen atoms in proteins and lipids were constrained using the SHAKE and RATTLE algorithms[82,83].

Nonbonded interactions were computed following standard CHARMM procedures. Lennard–Jones interactions were smoothly switched off between 10 and 12 Å using a force-based switching function, and electrostatic interactions were calculated using the particle mesh Ewald method[84,85]. The production runs employed the r-RESPA multiple time-step scheme with time steps of 2.5 and 5.0 fs for real-space and reciprocal-space interactions, respectively[86]. Finally, 200 ns of unrestrained molecular dynamics simulations were carried out for each membrane system. All simulations were performed using GENESIS version 2.1[30–32]

Cell culture and generation of stable cell lines

Claudin-null epithelial cells were previously established as described by Shigetomi et al.[8]. L929 fibroblast cells and claudin-null cells were maintained in Dulbecco's Modified Eagle's Medium supplemented with 10% fetal bovine serum (Sigma-Aldrich) at 37 °C in a humidified atmosphere containing 5% CO_2. Claudin-null cells were stably transfected with expression constructs encoding wild-type human claudin-4 (WT), the L1-site mutant claudin-4 (M29A), or the L2-site mutant claudin-4 (R81A). Stable cell lines were generated by antibiotic selection and maintained under continuous selection.

Immunofluorescence staining

Cells were cultured on glass coverslips and fixed with 3% formaldehyde in phosphate-buffered saline (PBS) for 10 min at room temperature (RT). After fixation, cells were permeabilized with 0.2% Triton X-100 in PBS for 5 min and washed three times with PBS. Non-specific binding was blocked by incubation with 5% bovine serum albumin in PBS for 30 min at RT. Primary antibodies were diluted in the blocking solution and applied to the cells for 1 h at RT. After washing with PBS, cells were incubated with appropriate fluorophore-conjugated secondary antibodies for 1 h at RT. For visualization of filamentous actin, Alexa Fluor 488-conjugated phalloidin (Life Technologies) was added during the secondary antibody incubation. After final washes with PBS, coverslips were mounted using an antifade mounting medium. Immunofluorescence samples were observed using a laser-scanning confocal microscope (LSM900; Carl Zeiss MicroImaging) equipped with a Plan-Apochromat oil-immersion objective lens (63×, numerical aperture 1.40). Image acquisition parameters, including pixel binning and exposure time, were optimized and kept constant within each experiment. All images were processed and analyzed using ZEN 2012 software (Carl Zeiss MicroImaging).

References

1. Furuse, M., Fujita, K., Hiiragi, T., Fujimoto, K. & Tsukita, S. Claudin-1 and -2: Novel Integral Membrane Proteins Localizing at Tight Junctions with No Sequence Similarity to Occludin. *J. Cell Biol.* **141**, 1539–1550 (1998).
2. Tsukita, S., Furuse, M. & Itoh, M. Multifunctional strands in tight junctions. *Nat. Rev. Mol. Cell Biol.* **2**, 285–293 (2001).
3. Mineta, K. *et al.* Predicted expansion of the claudin multigene family. *FEBS Lett.* **585**, 606–612 (2011).
4. Lambert, D., O'Neill, C. A. & Padfield, P. J. Depletion of Caco-2 cell cholesterol disrupts barrier function by altering the detergent solubility and distribution of specific tight-junction proteins. *Biochem. J.* **387**, 553–560 (2005).
5. Nusrat, A. *et al.* Tight junctions are membrane microdomains. *J. Cell Sci.* **113**, 1771–1781 (2000).
6. Lambert, D., O'Neill, C. & Padfield, P. Methyl-β-Cyclodextrin Increases Permeability of Caco-2 Cell Monolayers by Displacing Specific Claudins from Cholesterol Rich Domains Associated with Tight Junctions. *Cell. Physiol. Biochem.* **20**, 495–506 (2007).
7. Shigetomi, K., Ono, Y., Inai, T. & Ikenouchi, J. Adherens junctions influence tight

junction formation via changes in membrane lipid composition. *J. Cell Biol.* **217**, 2373–2381 (2018).

8. Shigetomi, K., Ono, Y., Matsuzawa, K. & Ikenouchi, J. Cholesterol-rich domain formation mediated by ZO proteins is essential for tight junction formation. *Proc. Natl. Acad. Sci.* **120**, e2217561120 (2023).
9. Gonschior, H. *et al.* Nanoscale segregation of channel and barrier claudins enables paracellular ion flux. *Nat. Commun.* **13**, 4985 (2022).
10. Shashikanth, N. *et al.* Tight junction channel regulation by interclaudin interference. *Nat. Commun.* **13**, 3780 (2022).
11. Kashihara, H. *et al.* Functional landscape of mechanistic diversity in 27 claudin family members at tight junctions. *Sci. Adv.* **11**, eadx7431 (2025).
12. Suzuki, H. *et al.* Crystal Structure of a Claudin Provides Insight into the Architecture of Tight Junctions. *Science* **344**, 304–307 (2014).
13. Saitoh, Y. *et al.* Structural insight into tight junction disassembly by *Clostridium perfringens* enterotoxin. *Science* **347**, 775–778 (2015).
14. Shinoda, T. *et al.* Structural basis for disruption of claudin assembly in tight junctions by an enterotoxin. *Sci. Rep.* **6**, 33632 (2016).
15. Nakamura, S. *et al.* Morphologic determinant of tight junctions revealed by claudin-

3 structures. *Nat. Commun.* **10**, 816 (2019).

16. Vecchio, A. J. & Stroud, R. M. Claudin-9 structures reveal mechanism for toxin-induced gut barrier breakdown. *Proc. Natl. Acad. Sci.* **116**, 17817–17824 (2019).

17. Suzuki, H., Tani, K., Tamura, A., Tsukita, S. & Fujiyoshi, Y. Model for the Architecture of Claudin-Based Paracellular Ion Channels through Tight Junctions. *J. Mol. Biol.* **427**, 291–297 (2015).

18. Irudayanathan, F. J., Trasatti, J. P., Karande, P. & Nangia, S. Molecular Architecture of the Blood Brain Barrier Tight Junction Proteins–A Synergistic Computational and *In Vitro* Approach. *J. Phys. Chem. B* **120**, 77–88 (2016).

19. Alberini, G., Benfenati, F. & Maragliano, L. A refined model of claudin-15 tight junction paracellular architecture by molecular dynamics simulations. *PLOS ONE* **12**, e0184190 (2017).

20. Rajagopal, N., Irudayanathan, F. J. & Nangia, S. Computational Nanoscopy of Tight Junctions at the Blood–Brain Barrier Interface. *Int. J. Mol. Sci.* **20**, 5583 (2019).

21. Nagarajan, S. K., Klein, S., Fadakar, B. S. & Piontek, J. Claudin-10b cation channels in tight junction strands: Octameric-interlocked pore barrels constitute paracellular channels with low water permeability. *Comput. Struct. Biotechnol. J.* **21**, 1711–1727 (2023).

22. Van Der Veen, R. E. *et al.* Claudin-4 polymerizes after a small extracellular claudin-3-like substitution. *J. Biol. Chem.* **300**, 107693 (2024).

23. Fuladi, S., McGuinness, S., Shen, L., Weber, C. R. & Khalili-Araghi, F. Molecular mechanism of claudin-15 strand flexibility: A computational study. *J. Gen. Physiol.* **154**, e202213116 (2022).

24. Marsch, P., Rajagopal, N. & Nangia, S. Biophysics of claudin proteins in tight junction architecture: Three decades of progress. *Biophys. J.* **123**, 2363–2378 (2024).

25. Frauenfeld, J. *et al.* A saposin-lipoprotein nanoparticle system for membrane proteins. *Nat. Methods* **13**, 345–351 (2016).

26. Shinoda, T. *et al.* Cell-free methods to produce structurally intact mammalian membrane proteins. *Sci. Rep.* **6**, 30442 (2016).

27. Hashimoto, Y. *et al.* Efficacy and safety evaluation of claudin-4-targeted antitumor therapy using a human and mouse cross-reactive monoclonal antibody. *Pharmacol. Res. Perspect.* **4**, e00266 (2016).

28. Jumper, J. *et al.* Highly accurate protein structure prediction with AlphaFold. *Nature* **596**, 583–589 (2021).

29. Varadi, M. *et al.* AlphaFold Protein Structure Database: massively expanding the

structural coverage of protein-sequence space with high-accuracy models. *Nucleic Acids Res.* **50**, D439–D444 (2022).

30. Jung, J. *et al.* GENESIS: a hybrid-parallel and multi-scale molecular dynamics simulator with enhanced sampling algorithms for biomolecular and cellular simulations. *WIREs Comput. Mol. Sci.* **5**, 310–323 (2015).

31. Kobayashi, C. *et al.* GENESIS 1.1: A hybrid-parallel molecular dynamics simulator with enhanced sampling algorithms on multiple computational platforms. *J. Comput. Chem.* **38**, 2193–2206 (2017).

32. Jung, J. *et al.* GENESIS 2.1: High-Performance Molecular Dynamics Software for Enhanced Sampling and Free-Energy Calculations for Atomistic, Coarse-Grained, and Quantum Mechanics/Molecular Mechanics Models. *J. Phys. Chem. B* **128**, 6028–6048 (2024).

33. Irudayanathan, F. J. *et al.* Self-Assembly Simulations of Classic Claudins—Insights into the Pore Structure, Selectivity, and Higher Order Complexes. *J. Phys. Chem. B* **122**, 7463–7474 (2018).

34. Yuan, M. *et al.* ZDHHC12-mediated claudin-3 S-palmitoylation determines ovarian cancer progression. *Acta Pharm. Sin. B* **10**, 1426–1439 (2020).

35. Rajagopal, N., Irudayanathan, F. J. & Nangia, S. Palmitoylation of Claudin-5

Proteins Influences Their Lipid Domain Affinity and Tight Junction Assembly at the Blood–Brain Barrier Interface. *J. Phys. Chem. B* **123**, 983–993 (2019).

36. Furuse, M. *et al.* Reconstitution of functional tight junctions with individual claudin subtypes in epithelial cells. *Cell Struct. Funct.* **48**, 1–17 (2023).

37. Lee, A. G. How lipids and proteins interact in a membrane: a molecular approach. *Mol. Biosyst.* **1**, 203 (2005).

38. Wattenhofer, M. *et al.* Different mechanisms preclude mutant CLDN14 proteins from forming tight junctions in vitro. *Hum. Mutat.* **25**, 543–549 (2005).

39. Zhao, J. *et al.* Multiple claudin–claudin cis interfaces are required for tight junction strand formation and inherent flexibility. *Commun. Biol.* **1**, 50 (2018).

40. Kausalya, P. J. Disease-associated mutations affect intracellular traffic and paracellular Mg2+ transport function of Claudin-16. *J. Clin. Invest.* **116**, 878–891 (2006).

41. Hempel, C. *et al.* Assembly of Tight Junction Strands: Claudin-10b and Claudin-3 Form Homo-Tetrameric Building Blocks that Polymerise in a Channel-Independent Manner. *J. Mol. Biol.* **432**, 2405–2427 (2020).

42. Van Itallie, C. M., Gambling, T. M., Carson, J. L. & Anderson, J. M. Palmitoylation of claudins is required for efficient tight-junction localization. *J. Cell Sci.* **118**,

1427–1436 (2005).

43. Zidar, J. *et al.* Liquid-Ordered Phase Formation in Cholesterol/Sphingomyelin Bilayers: All-Atom Molecular Dynamics Simulations. *J. Phys. Chem. B* **113**, 15795–15802 (2009).

44. Lingwood, D. & Simons, K. Lipid Rafts As a Membrane-Organizing Principle. *Science* **327**, 46–50 (2010).

45. Piontek, J., Krug, S. M., Protze, J., Krause, G. & Fromm, M. Molecular architecture and assembly of the tight junction backbone. *Biochim. Biophys. Acta BBA - Biomembr.* **1862**, 183279 (2020).

46. Marheineke, K., Grünewald, S., Christie, W. & Reiländer, H. Lipid composition of *Spodoptera frugiperda* (Sf9) and *Trichoplusia ni* (Tn) insect cells used for baculovirus infection. *FEBS Lett.* **441**, 49–52 (1998).

47. Dawaliby, R. *et al.* Phosphatidylethanolamine Is a Key Regulator of Membrane Fluidity in Eukaryotic Cells. *J. Biol. Chem.* **291**, 3658–3667 (2016).

48. Novak, M. *et al.* Binding specificity of ostreolysin A6 towards Sf9 insect cell lipids. *Biochim. Biophys. Acta BBA - Biomembr.* **1862**, 183307 (2020).

49. Madara, J. L. Increases in guinea pig small intestinal transepithelial resistance induced by osmotic loads are accompanied by rapid alterations in absorptive-cell

tight-junction structure. *J. Cell Biol.* **97**, 125–136 (1983).

50. Oshima, T., Koseki, J., Chen, X., Matsumoto, T. & Miwa, H. Acid modulates the squamous epithelial barrier function by modulating the localization of claudins in the superficial layers. *Lab. Invest.* **92**, 22–31 (2012).

51. Ouban, A. & Arabi, T. Z. Expression of Claudins in Preneoplastic Conditions of the Gastrointestinal Tract: A Review. *Cancers* **15**, 4095 (2023).

52. Demchenko, E. A. *et al.* Cryo-electron tomography reveals paracellular claudin-15 pores at the tight junction. *Biophys. J.* **125**, 3787–3792 (2026).

53. Klar, J. *et al.* Altered paracellular cation permeability due to a rare CLDN10B variant causes anhidrosis and kidney damage. *PLOS Genet.* **13**, e1006897 (2017).

54. Bashir, R., Fatima, A. & Naz, S. Mutations in CLDN14 are associated with different hearing thresholds. *J. Hum. Genet.* **55**, 767–770 (2010).

55. Bashir, Z.-H. *et al.* Phenotypic variability of CLDN14 mutations causing DFNB29 hearing loss in the Pakistani population. *J. Hum. Genet.* **58**, 102–108 (2013).

56. Thorleifsson, G. *et al.* Sequence variants in the CLDN14 gene associate with kidney stones and bone mineral density. *Nat. Genet.* **41**, 926–930 (2009).

57. Claverie-Martín, F. *et al.* Claudin-19 Mutations and Clinical Phenotype in Spanish Patients with Familial Hypomagnesemia with Hypercalciuria and Nephrocalcinosis.

PLoS ONE **8**, e53151 (2013).

58. Cho, H.-S. *et al.* Structure of the extracellular region of HER2 alone and in complex with the Herceptin Fab. *Nature* **421**, 756–760 (2003).

59. Terada, T., Murata, T., Shirouzu, M. & Yokoyama, S. Cell-free expression of protein complexes for structural biology. *Methods Mol. Biol. Clifton NJ* **1091**, 151–159 (2014).

60. Katsura, K. *et al.* A reproducible and scalable procedure for preparing bacterial extracts for cell-free protein synthesis. *J. Biochem. (Tokyo)* **162**, 357–369 (2017).

61. Yabuki, T. *et al.* A robust two-step PCR method of template DNA production for high-throughput cell-free protein synthesis. *J. Struct. Funct. Genomics* **8**, 173–191 (2007).

62. Matsuda, T. *et al.* Cell-free synthesis of functional antibody fragments to provide a structural basis for antibody–antigen interaction. *PLOS ONE* **13**, e0193158 (2018).

63. Kabsch, W. *XDS*. *Acta Crystallogr. D Biol. Crystallogr.* **66**, 125–132 (2010).

64. Collaborative Computational Project, Number 4. The CCP4 suite: programs for protein crystallography. *Acta Crystallogr. D Biol. Crystallogr.* **50**, 760–763 (1994).

65. Liebschner, D. *et al.* Macromolecular structure determination using X-rays, neutrons and electrons: recent developments in *Phenix*. *Acta Crystallogr. Sect. Struct. Biol.*

75, 861–877 (2019).

66. Emsley, P. & Cowtan, K. *Coot* : model-building tools for molecular graphics. *Acta Crystallogr. D Biol. Crystallogr.* **60**, 2126–2132 (2004).

67. McCoy, A. J. *et al. Phaser* crystallographic software. *J. Appl. Crystallogr.* **40**, 658–674 (2007).

68. Chen, V. B. *et al. MolProbity* : all-atom structure validation for macromolecular crystallography. *Acta Crystallogr. D Biol. Crystallogr.* **66**, 12–21 (2010).

69. Zivanov, J. *et al.* New tools for automated high-resolution cryo-EM structure determination in RELION-3. *eLife* **7**, e42166 (2018).

70. Punjani, A., Rubinstein, J. L., Fleet, D. J. & Brubaker, M. A. cryoSPARC: algorithms for rapid unsupervised cryo-EM structure determination. *Nat. Methods* **14**, 290–296 (2017).

71. Pettersen, E. F. *et al.* UCSF Chimera—A visualization system for exploratory research and analysis. *J. Comput. Chem.* **25**, 1605–1612 (2004).

72. Sanchez-Garcia, R. *et al.* DeepEMhancer: a deep learning solution for cryo-EM volume post-processing. *Commun. Biol.* **4**, 874 (2021).

73. Humphrey, W., Dalke, A. & Schulten, K. VMD: Visual molecular dynamics. *J. Mol. Graph.* **14**, 33–38 (1996).

74. Huang, J. *et al.* CHARMM36m: an improved force field for folded and intrinsically disordered proteins. *Nat. Methods* **14**, 71–73 (2017).

75. Price, D. J. & Brooks, C. L. A modified TIP3P water potential for simulation with Ewald summation. *J. Chem. Phys.* **121**, 10096–10103 (2004).

76. Bussi, G., Donadio, D. & Parrinello, M. Canonical sampling through velocity rescaling. *J. Chem. Phys.* **126**, 014101 (2007).

77. Martyna, G. J., Tuckerman, M. E., Tobias, D. J. & Klein, M. L. Explicit reversible integrators for extended systems dynamics. *Mol. Phys.* **87**, 1117–1157 (1996).

78. Jung, J., Kobayashi, C. & Sugita, Y. Optimal Temperature Evaluation in Molecular Dynamics Simulations with a Large Time Step. *J. Chem. Theory Comput.* **15**, 84–94 (2019).

79. Jung, J. & Sugita, Y. Group-based evaluation of temperature and pressure for molecular dynamics simulation with a large time step. *J. Chem. Phys.* **153**, 234115 (2020).

80. Lippert, R. A. *et al.* Accurate and efficient integration for molecular dynamics simulations at constant temperature and pressure. *J. Chem. Phys.* **139**, 164106 (2013).

81. Miyamoto, S. & Kollman, P. A. Settle: An analytical version of the SHAKE and

RATTLE algorithm for rigid water models. *J. Comput. Chem.* **13**, 952–962 (1992).

82. Ryckaert, J.-P., Ciccotti, G. & Berendsen, H. J. C. Numerical integration of the cartesian equations of motion of a system with constraints: molecular dynamics of n-alkanes. *J. Comput. Phys.* **23**, 327–341 (1977).

83. Andersen, H. C. Rattle: A "velocity" version of the shake algorithm for molecular dynamics calculations. *J. Comput. Phys.* **52**, 24–34 (1983).

84. Essmann, U. *et al.* A smooth particle mesh Ewald method. *J. Chem. Phys.* **103**, 8577–8593 (1995).

85. Darden, T., York, D. & Pedersen, L. Particle mesh Ewald: An $N \cdot \log(N)$ method for Ewald sums in large systems. *J. Chem. Phys.* **98**, 10089–10092 (1993).

86. Tuckerman, M., Berne, B. J. & Martyna, G. J. Reversible multiple time scale molecular dynamics. *J. Chem. Phys.* **97**, 1990–2001 (1992).

87. Katoh, K., Rozewicki, J. & Yamada, K. D. MAFFT online service: multiple sequence alignment, interactive sequence choice and visualization. *Brief. Bioinform.* **20**, 1160–1166 (2019).

88. Lomize, A. L., Todd, S. C. & Pogozheva, I. D. Spatial arrangement of proteins in planar and curved membranes by PPM 3.0. *Protein Sci.* **31**, 209–220 (2022).

Acknowledgments

The cryo-EM experiments were performed at the RIKEN Yokohama cryo-EM facility (R-COMS_IMS). We thank K. Hasegawa and H. Okumura (BL41XU), as well as the staff of BL26B2 at the Japan Synchrotron Radiation Research Institute (JASRI), SPring-8, for X-ray data collection. We also thank H. Shigematsu, T. Yokoyama, T. Uchikubo-Kamo, R. Akasaka, and A. Yamagata for assistance with cryo-EM data collection and analysis; K. Ihara for assistance with X-ray data analysis; O. Ohara (Kazusa DNA Research Institute) for the generous gift of cDNA clones; M. Inoue for plasmid preparation; and M. Yonemochi, S. Kohno, M. Ikeda, M. Goto, Y. Tomabechi, Y. Ishizuka, and K. Ito for protein sample preparation.

Synchrotron radiation experiments were conducted at BL26B2 and BL41XU of SPring-8 with the approval of RIKEN and JASRI (proposal numbers 2016A2511 and 2015B2085), respectively. This work was supported by the Platform Project for Supporting Drug Discovery and Life Science Research (Platform for Drug Discovery, Informatics, and Structural Life Science) from the Ministry of Education, Culture, Sports, Science and Technology (MEXT) and the Japan Agency for Medical Research and Development (AMED) (M.S.); by a Grant-in-Aid for Scientific Research (C) (JP18K06100) from MEXT (T.S.); by Health and Labour Sciences Research

Grant (H23-Seisaku-Ippan-008) from the Ministry of Health, Labour and Welfare (M.K.); in part by the RIKEN Pioneering Project “Biology of Intracellular Environments” (Y.S., M.S.); and in part by the RIKEN–Kyushu University Science and Technology Hub Collaborative Research Program and the RIKEN Cluster for Science, Technology and Innovation Hub (T.S., J.I.). AI-assisted language editing was performed using ChatGPT (GPT-5.3; OpenAI) to improve the readability of this manuscript.

Author contributions

T.S., J.I., Y.S., T.K.-S., M.K. and M.S. designed the research. K.H. prepared the protein expression plasmids. T.S. and N.S. performed protein expression, purification and crystallization. K.S. and J.I. performed cellular experiments. M.M. and Y.S. performed MD simulation. K.K. performed cryo-EM data collection and assisted with the cryo-EM data analysis. T.S. performed X-ray data collection, X-ray data analysis, cryo-EM data analysis and structure determination. T.S., M.M., J.I., Y.S. and M.S. wrote the manuscript. Correspondence and requests for materials should be addressed to T.S. (takehiro.shinoda@riken.jp) and M.S. (mikako.shirouzu@riken.jp).

Competing interests

The authors declare no conflicts of interest related to the content of this article.

Data and materials availability

The cryo-EM map and atomic coordinates have been deposited in the Electron Microscopy Data Bank (EMDB) and the Protein Data Bank (PDB) under accession codes EMD-69645 and 24MB, respectively, for human claudin-4 in complex with an anti-claudin-4 Fab fragment, and 24LZ for the chimeric Fab fragment of the anti-claudin-4 antibody 5D12. All data supporting the findings of this study are available in the main text or in the supplementary materials.

Figures legends

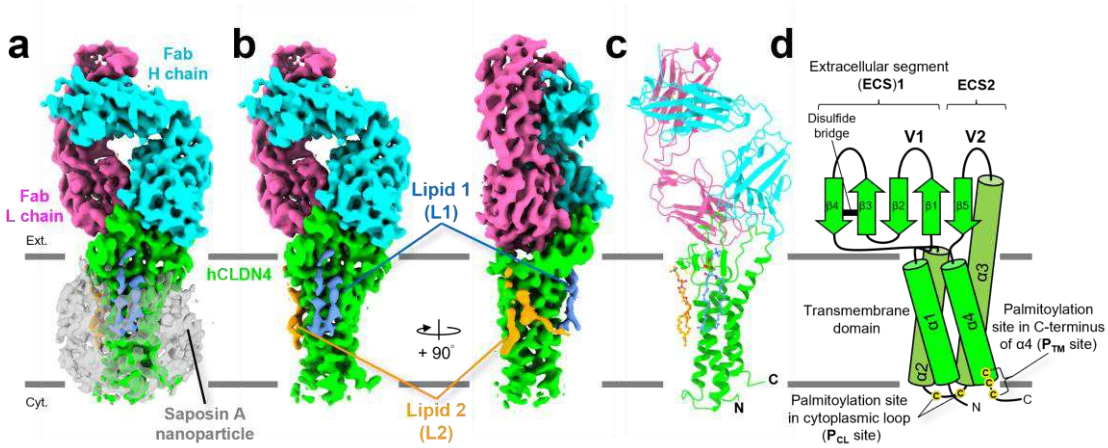


Fig. 1 | Cryo-EM structure of human claudin-4 in complex with an anti-claudin-4 Fab fragment and two bound lipids.

a, b, Cryo-EM density maps of human claudin-4 (hCLDN4) in complex with a chimeric Fab fragment of an anti-hCLDN4 antibody (clone 5D12[27]), (**a**) with and (**b**) without a saposin A nanoparticle. Density maps are visualized using Chimera X and contoured at a level of 0.35. **c,** Cartoon representation of the cryo-EM structure showing two bound lipid molecules, lipid 1 (L1) and lipid 2 (L2). **d,** Schematic representation of the consensus secondary structure of claudin.

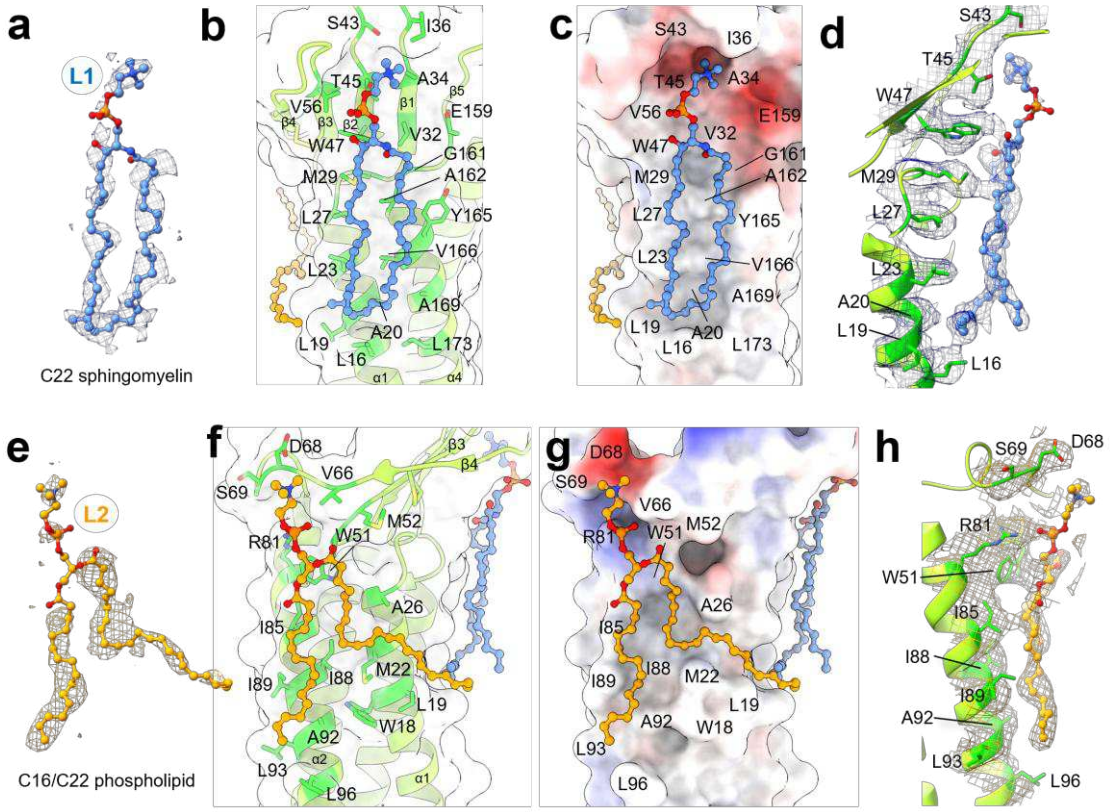


Fig. 2 | Two bound lipids revealed by the cryo-EM structure of human claudin-4.

Structural details of the L1 (**a–d**) and L2 (**e–h**) lipid-binding sites in human claudin-4 (hCLDN4). **a, e,** Cartoon representations of the bound lipids on hCLDN4. Cryo-EM density maps are shown as meshes contoured at 0.45 and visualized using ChimeraX. The bound lipids are shown in blue (L1) and orange (L2) in ball-and-stick representation. **b, f,** Cartoon representations of the hCLDN4 cryo-EM structure highlighting the lipid-binding sites. Residues within 5.0 Å of the bound lipids are labeled. **c, g,** Electrostatic surface representations of the lipid-binding sites, viewed from the same orientations as in **b** and **f**, respectively. Electrostatic potentials were calculated

using ChimeraX and are color-coded from −10 kT/e (red) to +10 kT/e (blue). **d, h,** Lateral views of the lipid-binding sites with cryo-EM density maps shown as meshes contoured at 0.45.

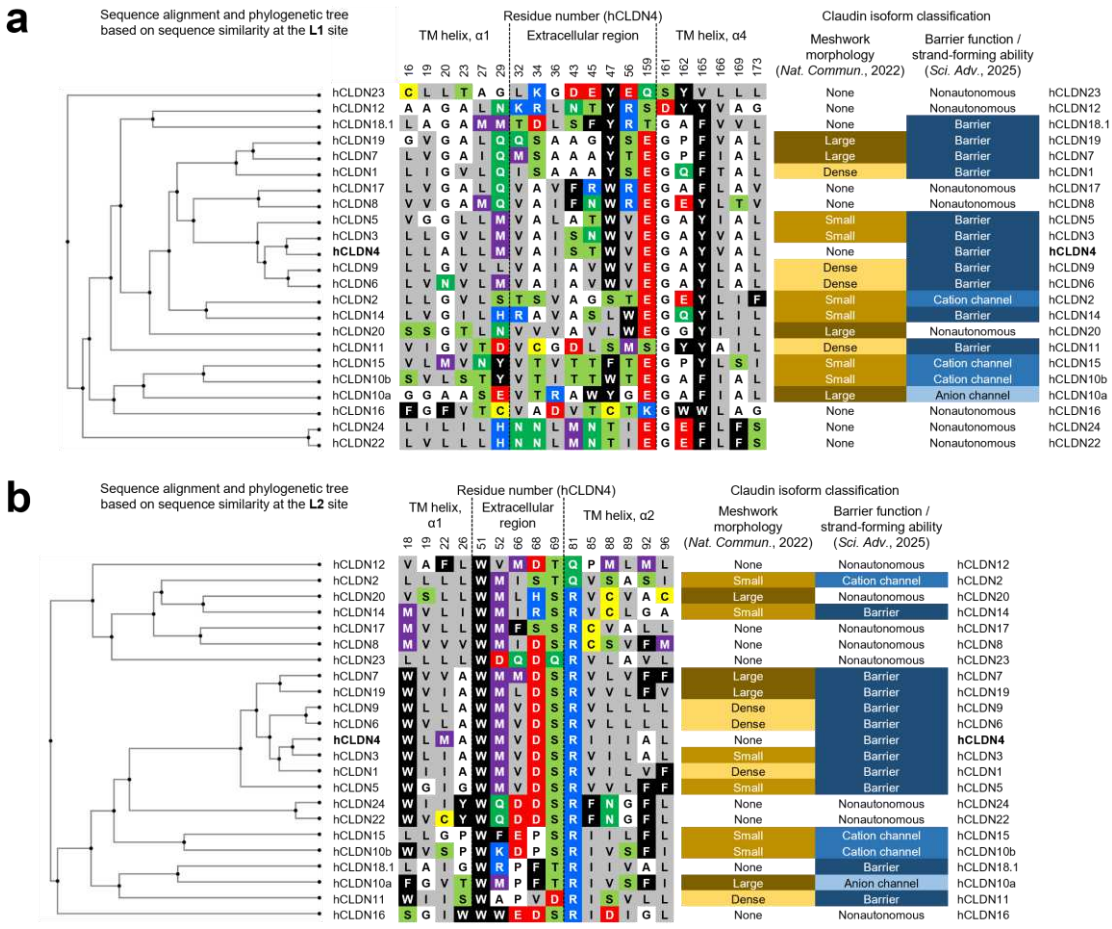


Fig. 3 | Comparison of isoform classification based on sequence similarity at the lipid-binding sites with previously reported classifications.

Sequence alignments and phylogenetic trees in the left columns, based on sequence similarity at the (**a**) L1 and (**b**) L2 sites, were generated using MAFFT[87] from residues at the L1 and L2 sites extracted from the multiple sequence alignment of human claudin isoforms (Supplementary Fig. 4). Claudin isoforms are classified in the right columns according to meshwork morphology[9] (Large, Small, Dense: isoforms forming large, small, and dense meshworks, respectively; None: isoforms not forming meshworks) and

barrier function and strand-forming ability[11] (Barrier: autonomous TJ barriers; Cation and Anion channel: forming autonomous TJ barrier-based cation or anion channels; Nonautonomous: not forming autonomous TJ barriers).

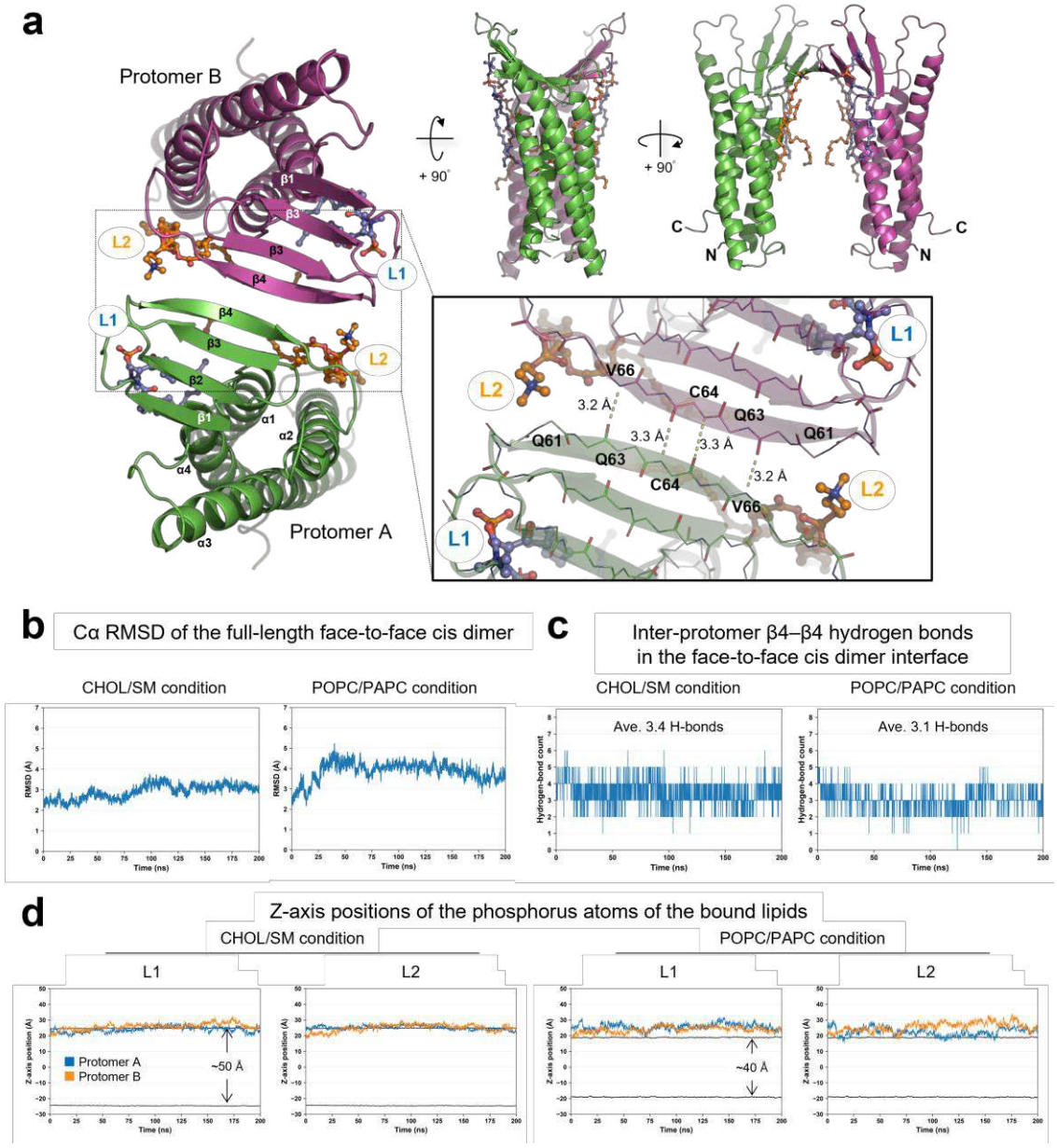


Fig. 4 | Molecular dynamics simulations of the human claudin-4 face-to-face cis dimer in lipid membrane environments.

a, Cartoon representation of the human claudin-4 (hCLDN4) face-to-face cis dimer with bound lipids used as the initial model for the MD simulations. **b–d,** MD simulation analyses of the hCLDN4 dimer under two different membrane conditions. All

simulations were performed for 200 ns under unrestricted conditions. **b,** Root-mean-square deviation (RMSD) of Cα atoms of the hCLDN4 dimer, indicating the extent of conformational deviation over time. **c,** Number of hydrogen bonds at the face-to-face cis dimer interface during the simulations. **d,** z-axis positions of the phosphorus atoms of the bound lipids, L1 and L2. The average z-positions of the phosphorus atoms of bulk membrane lipids are indicated by solid black lines.

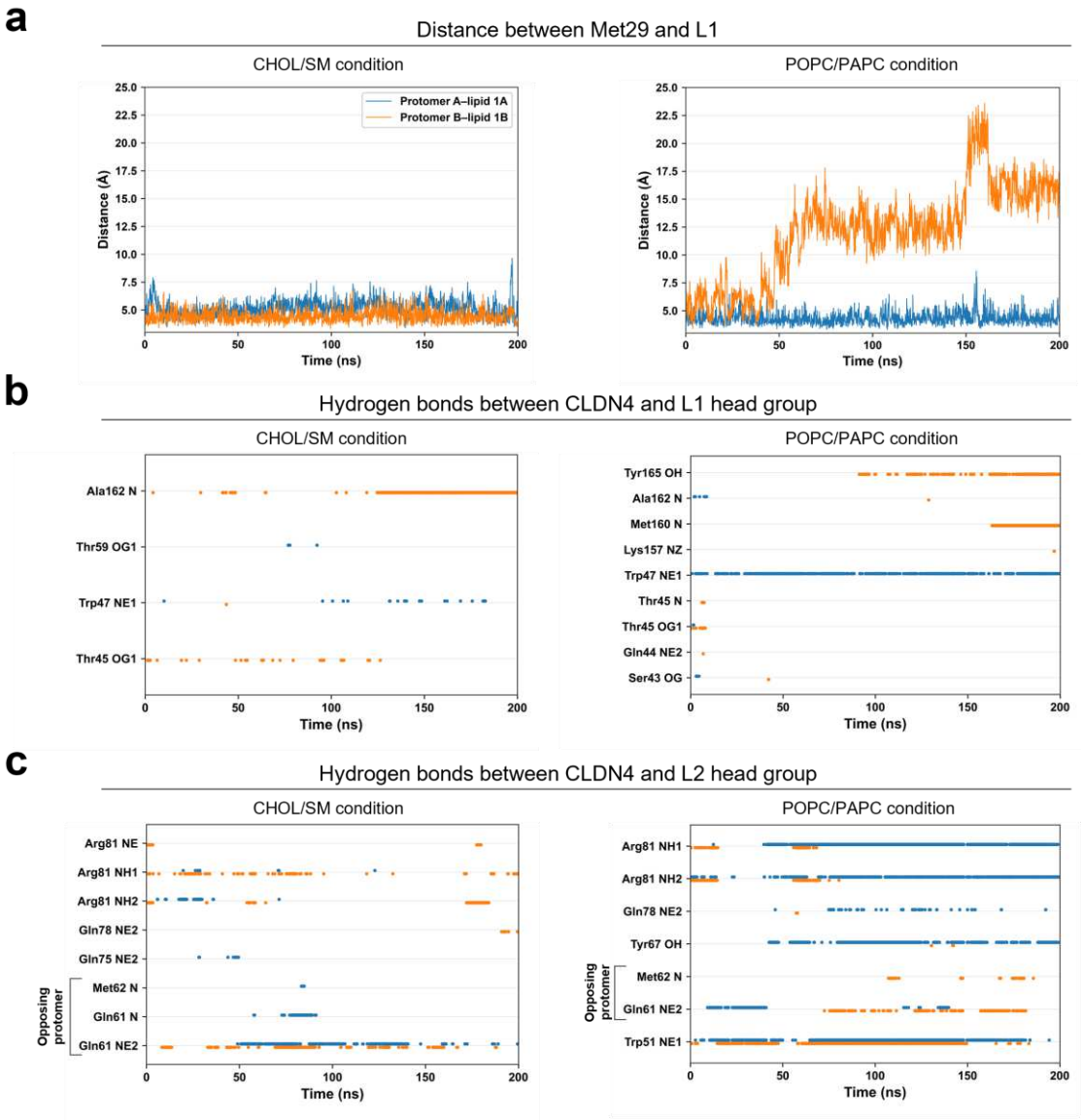


Fig. 5 | Molecular dynamics analysis of claudin-4–lipid interactions.

Interactions between the human claudin-4 (hCLDN4) face-to-face cis dimer and the two bound lipids, L1 and L2, under two different membrane conditions, as simulated in Fig. 4. **a,** Distance between Met29 of hCLDN4 and L1 during the MD simulations. **b, c,** Hydrogen bond formation between the lipid head groups and claudin residues at the (**b**) L1 and (**c**) L2 sites over the 200-ns simulations.

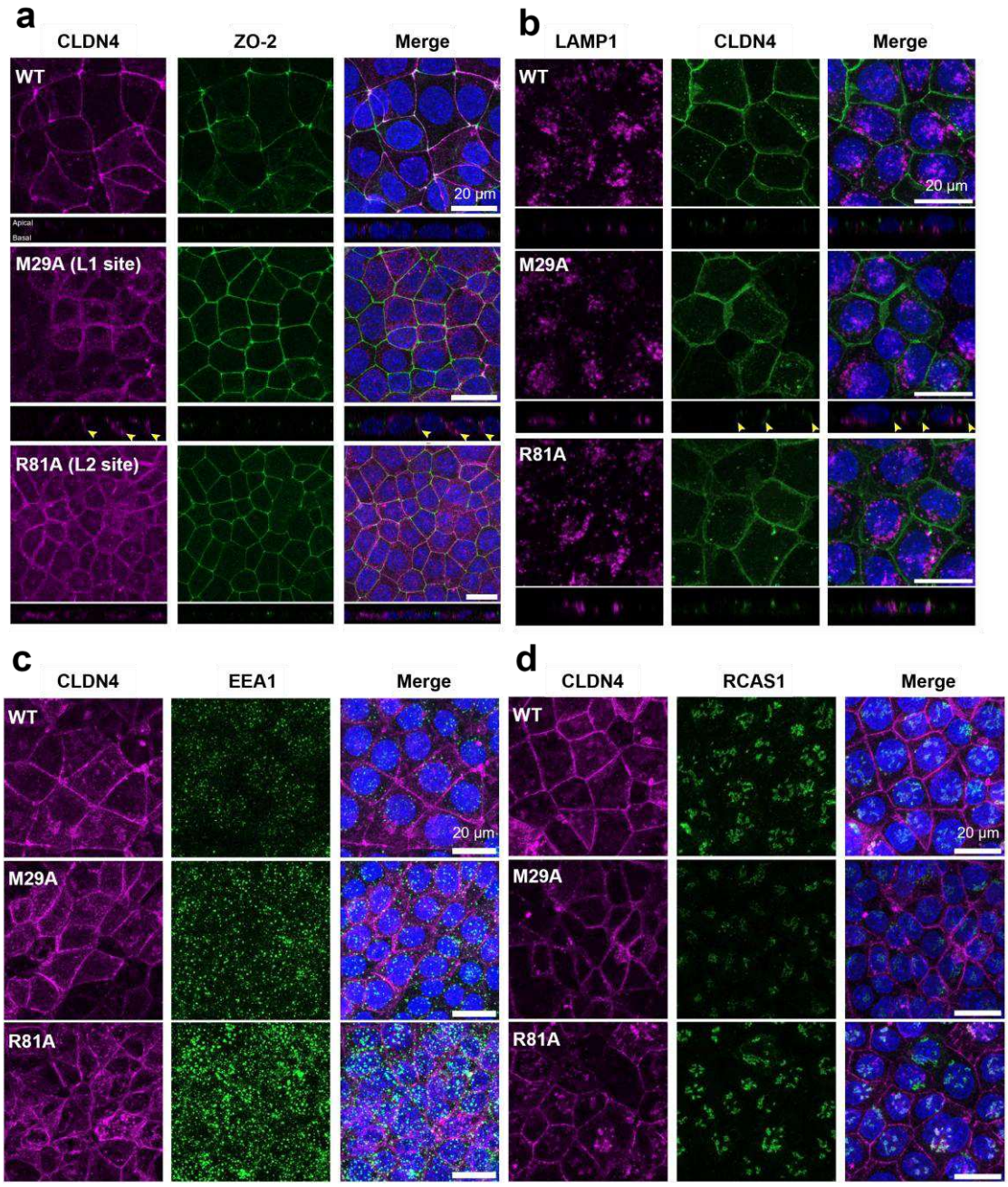


Fig. 6 | Phenotypic analysis of L1- and L2-site mutants of claudin-4 in claudin-null Eph4 cells.

Representative immunofluorescence images of claudin-null Eph4 cells expressing wild-type claudin-4 (WT) or the M29A and R81A mutants. Cells were stained for **a,** claudin-

4 (magenta) and ZO-2 (green); **b,** LAMP1 (magenta), a lysosomal marker, and claudin-4 (green); **c,** claudin-4 (magenta) and EEA1 (green), an early endosome marker; and **d,** claudin-4 (magenta) and RCAS1 (green), a cis-/medial-Golgi marker. Merged images including DAPI nuclear staining are shown in the rightmost column. Yellow arrowheads in (**a, b**) indicate the M29A mutant retained at the lateral membrane. Scale bar, 20 μm.

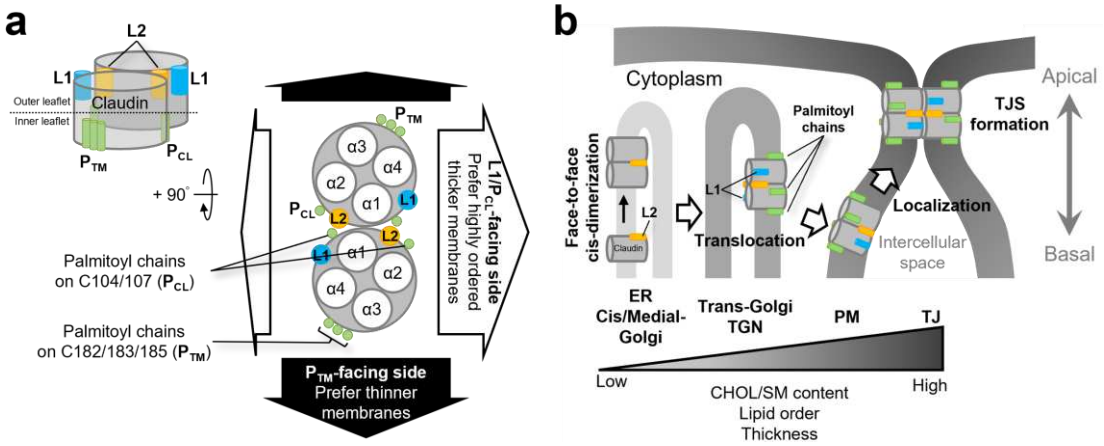


Fig. 7 | Membrane environment-dependent claudin translocation and tight junction localization.

a, Bipolar lipid preferences of the face-to-face cis claudin dimer generated by bound lipids (L1 and L2) and palmitoylation, resulting in asymmetric membrane environments around the dimer. **b,** Schematic model illustrating intracellular claudin translocation and apical tight junction localization along a cholesterol/sphingomyelin (CHOL/SM) gradient across cellular membranes.

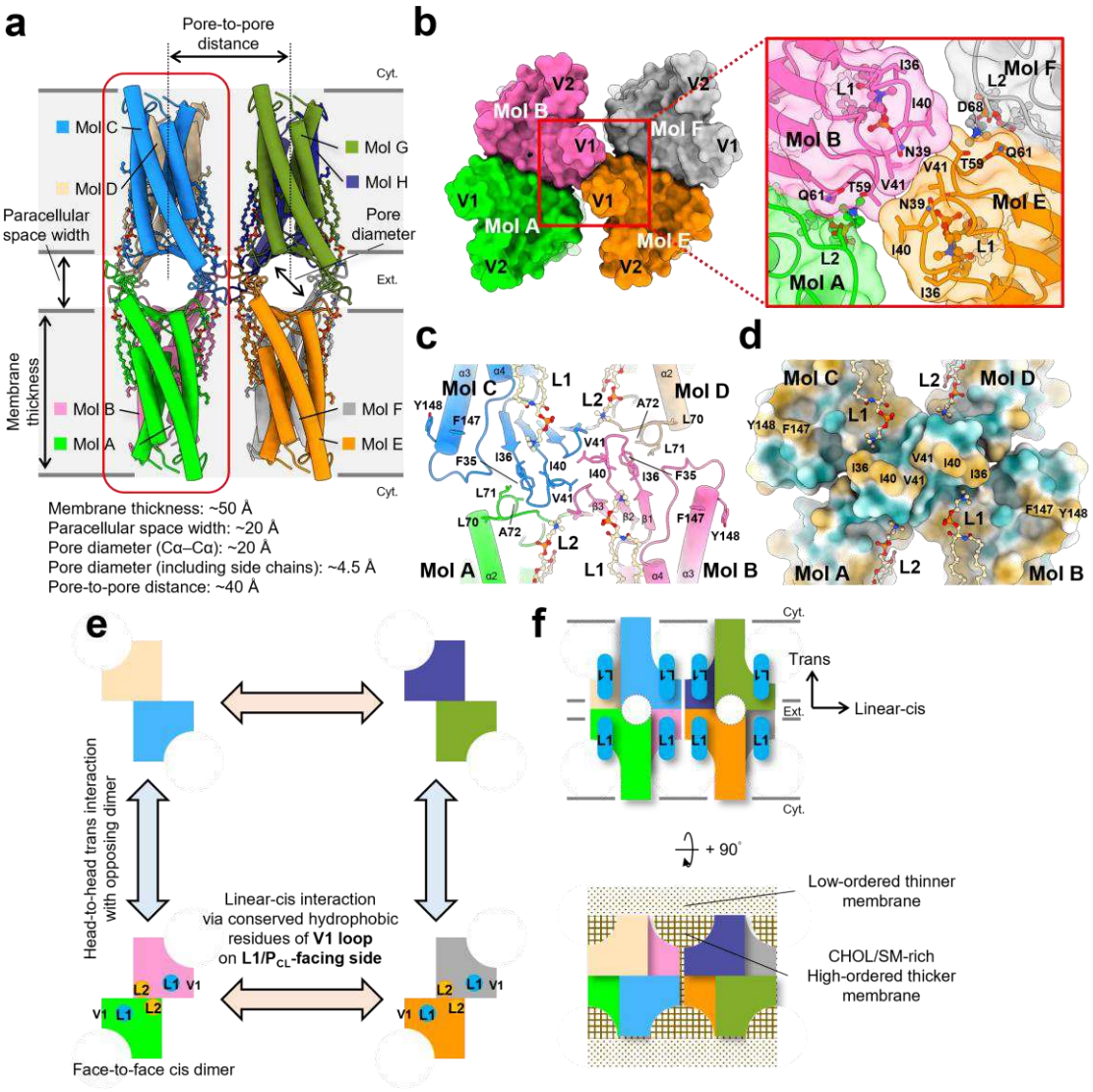


Fig. 8 | Membrane environment-dependent tight junction strand formation.

a–d, Hypothetical octameric claudin-4 strand model incorporating the two bound lipids (L1 and L2) identified in the cryo-EM structure. **a,** Overall view of the strand model viewed from the pore side. The tetrameric unit, representing the minimal functional unit, is indicated by a red box. The membrane thickness is based on our MD simulation results (Fig. 4d), and the paracellular space width was estimated from the distance

between the z-axis positions of the phosphorus atoms of opposing L1 lipids. **b,** Linear-cis interactions between claudin molecules aligned within the same membrane plane. The extracellular view of Mol A, B, E, and F forming the octameric strand shown in (**a**) is presented. An enlarged view highlights the contact interface at the V1 regions between Mol B and E. **c, d,** Interunit interfaces within the strand model shown in (**a**), represented as (**c**) a cartoon model and (**d**) a hydrophobic surface potential map, color-coded from hydrophobic regions (orange) to hydrophilic regions (light blue). **e, f,** Conceptual models illustrating (**e**) linear-cis and trans interactions of claudins driven by the bipolar lipid preferences of the face-to-face cis dimer, and (**f**) the resulting octameric tight junction strand architecture assembled through these interactions.

Supplementary Files

This is a list of supplementary files associated with this preprint. Click to download.

- 20261023ShinodaNCOMMSSIfinal.docx